An Cretaceous carbonate replacement origin for the Xinqiao stratabound massive sulfide deposit, Middle-Lower Yangtze Metallogenic Belt, China

Yang Li[1, 2 †], Jian-Wei Li[1], Xian-Hua Li[3], David Selby[2], Guang-Huan Huang[1], Lin-Jie Chen[4] and Kai Zheng[4]

[1] Faculty of Earth Resources, China University of Geosciences, Wuhan, 430074, China

[2]Department of Earth Sciences, Durham University, Durham, DH1 3LE, UK

[3]State Key Laboratory of Lithospheric Evolution, Institute of Geology and Geophysics, Chinese Academy of Sciences, Beijing, 100029, China

[4]321 Geological Team, Bureau of Geology and Mineral Exploration of Anhui province, Tongling, 244033, China

[†] Corresponding author Email, li.yang@durham.ac.uk, cugliyang@126.com

Abstract

Stratabound massive sulfide deposits are widespread along the Middle-Lower Yangtze Metallogenic Belt (MLYMB) and serve as an important copper producer in China. Two contrasting genetic models have been proposed, interpreting the stratabound massive sulfide deposits as a Carboniferous SEDEX protore overprinted by Cretaceous magmatic-hydrothermal system or an Early Cretaceous carbonate replacement deposit. These two contrasting models have been applied to the Xinqiao stratabound Cu-Au sulfide deposit, which is dominated by massive sulfide ores hosted in marine carbonates of the Carboniferous Chuanshan and Huanglong Formations, with minor Cu-Au skarn ores localized in the contact zone between the Cretaceous diorite Jitou stock and the Carboniferous carbonate rocks. New SIMS zircon U-Pb dating suggests that the Jitou stock formed at 138.5 ± 1.1 Ma (2σ, MSWD = 0.6), whereas an unaltered diorite porphyry dike in the mine was emplaced at 130.6 ± 1.1 Ma (2σ, MSWD = 0.1). Pyrite Re-Os dating yields an imprecise date of 142 ± 47 Ma (2σ, MSWD = 7.8). The geochronological data thus constrain the mineralization of the Xinqiao deposit as early Cretaceous.

Fluid inclusions in prograde skarn diopside have homogenization temperatures of 450-600 ^{o}C and calculated salinities of 13-58 wt. % NaCl equiv. Quartz from the stratabound ores and pyrite-quartz vein networks beneath the stratabound ores have homogenization temperatures of 290-360 and 200-300 ^{o}C, with calculated salinities of 5-12 and 2-10 wt. % NaCl equiv., respectively. Quartz from the skarn ores and veins beneath the stratabound ores have δ^{18}O values of 12.32 ± 0.55 (2 SD, n = 22) and 15.57 ± 1.92 ‰ (2 SD, n = 60), respectively, corresponding to calculated δ^{18}Ovalues of 6.22 ± 1.59 (2σ) and 6.81 ± 2.76 ‰ (2σ) for the equilibrated ore-forming fluids. The fluid inclusion and oxygen isotope data thus support a magmatic-

hydrothermal origin rather than a SEDEX system for the stratabound ores, with the hydrothermal fluids most likely being derived from the Jitou stock or associated concealed intrusion. Results from this study have broad implications for the genesis and exploration of other stratabound massive sulfide deposits along the MLYMB.

Keywords

Stratabound Massive Sulfide Deposit, SIMS Oxygen Isotope, Zircon U-Pb, Pyrite Re-Os, Fluid Inclusion, Carbonate Replacement Deposit

Introduction

Stratabound massive sulfide deposits have been well documented in Mexico (Meinert 1982) and north-central Chile (Sato 1984), which have been commonly considered as carbonate replacement deposits (CRD). Equivalents of this type of deposits are widespread along the Middle-Lower Yangtze Metallogenic Belt (MLYMB), having been important copper producers in China during the last three decades (e.g., Pan and Dong 1999; Mao et al. 2011 and references therein). These deposits are predominantly hosted in Carboniferous carbonates, but show a close spatial association with Cretaceous granitoid intrusions that are genetically related to porphyry-skarn ores (Mao et al. 2011 and references therein). Despite many years of research, considerable debate remains on the genesis of these deposits (Guo et al. 2011; Mao et al. 2011; Xie et al. 2014; Xiao et al. 2016). Several studies advocate that the stratabound massive sulfide deposits are products of a Carboniferous sedimentary exhalative (SEDEX) system, which was overprinted by hydrothermal fluids associated with Cretaceous magmatism (Gu et al. 2000; Gu et al. 2007; Zhou et al. 2010; Guo et al. 2011; Xie et al. 2014; Xiao et al. 2016). In contrast, some authors considered these deposits as skarn/carbonate replacement systems genetically associated with Cretaceous magmatism (Pan and Dong 1999; Mao et al. 2011; Zhang et al. 2015). The contrasting genetic models have hampered recent mineral exploration strategies (Guo et al. 2011; Mao et al. 2011; Xie et al. 2014; Xiao et al. 2016).

The Wushan and Chengmenshan deposits in the Jiurui district, west MLYMB, and Dongguashan and Xinqiao deposits in the Tongling district, central MLYMB (Fig. 1) are the most important and representative stratabound massive sulfide deposits within this giant metallogenic belt. In these mining districts, stratabound orebodies are mostly hosted in Late Carboniferous limestone and dolomite and, to a lesser extent, in the Early Permian limestone. In

addition to the stratabound occurrence, the stratabound orebodies are characterized by laminated structures and local presence of colloform pyrite. Another striking feature is the development of vertical to sub-vertical pyrite-quartz vein networks beneath stratabound orebodies. These field observations indicate that Xinqiao deposit share many similarities with typical SEDEX deposits (Large 1983; Leach et al. 2004; Leach et al. 2005). On the other hand, most of the stratabound deposits show close spatial association with Cretaceous intrusions that also exhibit variable amounts of porphyry-skarn mineralization (Pan and Dong 1999; Gu et al. 2007; Mao et al. 2011). Coexistence of SEDEX textures and magmatic association has resulted in a prolonged debate about the genesis of those stratabound massive sulfide deposits (Pan and Dong 1999; Gu et al. 2007; Zhou et al. 2008; Guo et al. 2011; Mao et al. 2011; Xie et al. 2014; Zhang et al. 2015; Xiao et al. 2016).

In this paper, we present fluid inclusion, quartz oxygen isotope, zircon U-Pb and pyrite Re-Os data for the Xinqiao stratabound massive sulfide deposit. These new data are used to constrain the nature and origin of ore-forming fluids, emplacement age of the Cretaceous intrusions, and ultimately ore genesis. Combined with published geochemical and geochronological data, results from this study suggest a Cretaceous magmatic origin for the Xinqiao deposit. Our study also has implications for genesis of other stratabound massive sulfide deposits along MLYMB, and may offer guidance for future exploration within this metallogenic belt.

Geologic background

The MLYMB is located along the NE margin of the Yangtze craton that is separated from the Dabie Ultra-High Pressure Belt (UHP) by the Xiangfan-Guangji Fault in the north, and from

the North China craton by the Tancheng-Lujiang (Tan-Lu) Fault in the northeast (Fig. 1). The Changzhou-Yangxin and Guangde Faults define the southern and eastern boundaries of the MLYMB, respectively (Pan and Dong 1999).The northern Yangtze craton is underlain by tonalitic-trondjhemitic-granitic (TTG) gneisses and amphibolite to granulite facies supracrustal rocks (Zhao et al. 2011; Wan 2012). The TTG rocks have LA-ICP-MS zircon U-Pb ages ranging from 3.45 to 2.87 Ga (Guo et al. 2014). The TTG dominated basement rocks are unconformably overlain by Late Archean to Paleoproterozoic (2900-1895 Ma) calc-alkaline basalts, rhyolites, carbonate and clastic sedimentary rocks that metamorphosed to amphibolite and granulite facies (Pan and Dong 1999). Continent-rifting or subduction related magmatism occurred at 848 ± 4 Ma (Li et al. 2008). Caron-wide marine deposition occurred from the Cambrian to the Late Devonian and ceased during the Early Carboniferous as a result of uplift of the Yangtze craton (Pan and Dong 1999; Wan 2012). Subsidence of the Yangtze craton during the Late Carboniferous permitted further marine sedimentation until the Late Triassic (Wu et al. 2003; Wan 2012). The Proterozoic to Triassic strata have been pervasively affected by the Triassic Indosinian Orogeny involving the continental collision between the Indochina and South China blocks (Wu et al. 2003; Wan 2012).

Within the MLYMB, Late Silurian sandstones are unconformably overlain by sandstones of the Late Devonian Wutong Formation, which are unconformably overlain by sandstones of Early Carboniferous Gaolishan Formation. The Late Carboniferous Huanglong Formation dolomites and limestones are paraconformable lying above the Gaolishan Formation. Above the Huanglong Formation is Late Carboniferous Chuanshan Formation limestone. Paraconformably overlying the Chuanshan Formation is the Early Permian Qixia Formation, which comprises carbonaceous shales, siltstones and intercalated mudstones, carbonaceous limestone. Middle to Upper Permian

Maokou, Longtan and Dalong Formations are dominated by cherts, shales, calcareous shales, banded limestone, and layered limestone. The latter formations are overlain by Triassic sediments that are dominated by limestone, dolomite, clastic rocks (sandstone) and shales (Pan and Dong 1999).

Granitoid intrusions and volcanic rocks are widely distributed throughout the MLYMB (Fig. 1). These magmatic units are divided into two groups based on their formation ages and lithologies (Zhou et al. 2008; Mao et al. 2011). The first group is dominated by granitoid intrusions emplaced between 148 and 135 Ma, and is widely distributed in Daye, Jiurui, Anqing, Tongling and Ningzhen districts (Fig. 1). The second group is composed of volcanic and subvolcanic rocks formed between133 and 123 Ma, which are mostly distributed in Ningwu and Luzong volcanic basins (Fig. 1). Group one intrusions are dominated by quartz diorite, granodiorite, and monzonite, with subordinate gabbro, diorite, syenite and granite, and are associated with the majority of Cu-Au and Cu-Fe porphyry-skarn deposits throughout MLYMB (Zhou et al. 2008; Mao et al. 2011). In contrast, the second group volcanic-subvolcanic sequences are spatially and temporally related to the skarn and Kiruna-type iron deposits (Zhou et al. 2008; Mao et al. 2011).

A thrust fault is recognised broadly along the unconformity between Late Devonian sandstone and Early Carboniferous carbonates, which formed during the Triassic Indosinian Orogeny, and was reactivated during the Late Mesozoic Yanshan Orogeny associated with westward subduction of the paleo-Pacific plate (Li and Fu 1991; Wu et al. 2003; Li and Li 2007). This thrust system and its associated structures have a close spatial association with the Cretaceous intrusions and resultant porphyry-skarn Fe-Cu mineralization. In addition, almost all

the stratabound massive sulfide deposits in MLYMB occur along the thrust system (Wu et al. 2003).

Geology of the Xinqiao deposit

Stratigraphy

The stratigraphic column of sedimentary rocks exposed in the Xinqiao mine and surrounding areas is presented in Fig. 2 (803-Geological-Team 1971). The oldest rocks exposed are the Silurian sandstone and shales, which are unconformably overlain by the Late Devonian Wutong Formation. The Wutong Formation consists of pale-yellow quartz sandstone of 140 m thickness, with interbedded dark-grey shale and sandy shale. Quartz conglomerate with a thickness of 10-30 cm is present at the top of the Wutong Formation in the mining area (803-Geological-Team 1971).

The Early Carboniferous Gaolishan Formation has a thickness of 30-50 m and is paraconformable with the underlying Wutong Formation. The lower and middle Gaolishan Formation predominately consists of pale-yellow and pale quartz sandstone, while the upper part comprises fine-grained quartz conglomerate, siltstone, and silty shales. The upper part of the Gaolishan Formation is extensively fractured (Li and Fu 1991) and contains abundant pyrite-quartz veins with a volume percentage of 5-25, which represent the main host of Au at Xinqiao (803-Geological-Team 1971). Pyrite grains are generally euhedral or subeuhedral cubic crystals with a grain-size of 0.5-1 mm, but 2-5 mm grains are also documented (Guo et al. 2011).

Overlying the Gaolishan Formation is the Late Carboniferous Huanglong Formation which includes ~30 m of limestone, dolomitic limestone and dolomite with locally presented silty sandstone at the base of the formation. The main stratabound massive sulfide orebody is hosted

within the bottom part of the Huanglong Formation and above the Gaolishan Formation (Fig. 3; 803-Geological-Team 1971). Consequently, the bottom part of the Huanglong Formation is significantly replaced by the massive sulfide orebody, and in certain cases is completely replaced, as best illustrated near the Cretaceous Jitou stock (Fig. 3B and C).

The Late Carboniferous Chuanshan Formation is 60 m thick. The lower part of the Chuanshan Formation is dominated by limestone in paraconformable contact with the underlying Huanglong Formation. The upper part of the Chuanshan Formation comprises laminated limestone and fossiliferous clastic limestone.

Paracomformably overlying the Chuanshan Formation is the Early Permian Qixia Formation, which is composed of dark-grey carbonaceous limestone and grey cherty or nodular cherty limestone in the lower and upper parts, respectively.

Permian-Triassic limestone, calcareous shale, cherty shale, silty shale and sandstone are widely distributed in the mining area with a total thickness of > 350 m.

All the carbonates in the mining area experienced variable degrees of metamorphism associated with the emplacement of the Cretaceous intrusions discussed below (803-Geological-Team 1971). Siltstone and silty shales of the Gaolishan Formation, which serves as the footwall of the massive orebody, exhibit extensive sericitization, with locally distributed hornfels (803-Geological-Team 1971; Xu and Zhou 2001). The thrust system in Xinqiao mining area is broadly parallel to the unconformity between the Gaolishan and Huanglong Formations, and in some cases Chuanshan Formation carbonates are also part of this thrust system. Fault breccias are composed of limestone and silty shales, which have been thermally metamorphosed to marble and hornfels (803-Geological-Team 1971; Li and Fu 1991; Wu et al. 2003).

Igneous rocks

Magmatism in the Xinqiao mine is largely represented by the Cretaceous Jitou quartz diorite stock (Figs. 6A, B), with additional dikes and sills of similar compositions (Fig. 3; 803-Geological-Team 1971; Xu and Zhou 2001).

The Jitou stock intrudes the Permian-Triassic carbonates and has an outcrop of 0.3 km^2 (Fig. 3A). Drill-core logging indicate it extends northward at depth (Fig. 3B; 803-Geological-Team 1971). Though there is no obviously compositional variations across the pluton, but can be divided into a medium-grained central phase and a porphyritic marginal phase. The central phase (Fig. 3A) is dominated by quartz diorite (Fig. 6A) comprising plagioclase (60 vol. %), quartz (25 vol. %) and hornblende (9 vol. %) with minor alkali feldspar (4 vol. %) and biotite (1 vol. %), and accessory minerals including zircon, titanite, apatite and magnetite. The marginal phase is dominated by diorite porphyry (Fig. 6B) which comprises plagioclase (30 vol. %) and hornblende (20 vol. %) as phenocrysts, and groundmass dominated by plagioclase (25 vol. %), quartz (20 vol. %) and hornblende (2 vol. %), and accessory minerals that include apatite, titanite, zircon and magnetite. In addition, monzonite is also documented as a component of the marginal phase (Wu et al. 2009).

Several quartz diorite and porphyritic diorite dikes and sills are exposed or revealed via drill cores. The dikes and sills are compositionally and texturally similar to the marginal phase of the Jitou stock. The dikes and sills are particularly abundant in the northeast side of the Jitou stock (Fig. 3B), in the hanging-wall of the Qixia Formation, and along stratigraphic contacts. It is thought the Jitou stock provided a feeder for these dikes and sills (803-Geological-Team 1971). These dikes and sills, and the marginal phase of the Jitou stock as well, exhibit extensive alteration (see below), as indicated by feldspar dissolution (Fig. 6B).

A diorite porphyry dike was encountered during the mining activity in the southeast wall of the open pit (Fig. 6C). This dyke consists of plagioclase (27 vol. %) and hornblende (8 vol. %) as phenocrysts, with a groundmass predominately comprising plagioclase (48 vol. %) and quartz (15 vol. %), and accessory minerals that include pyrite, magnetite, apatite and zircon. No associated mineralization or alteration has been documented for this dike.

Mineralization and alteration

The Xinqiao deposit has an estimated resource of 10.22 million tonnes at an average of 0.938 % Cu and 34.87 % S, respectively. Greater than 90 % of the resource is hosted by the main stratabound-type orebody that is located along the lithological contact of Gaolishan and Huanglong Formations (Fig. 3; 803-Geological-Team 1971). It extends along a NE-strike for 2.56 km and average 21 m in thickness, with the thickest segments (~70 m) occurring in close proximity to the Jitou stock (Fig. 3; 803-Geological-Team 1971). Minor massive orebodies are fault hosted (Fig. 3B). The Xinqiao deposit average at 0.73 g/t Au,14.12 g/t Ag, and 0.5 % Zn, but the supergene zones, which has been mined out, contained up to 2 g/t Au and 70g/t Ag. The ore grades of the stratabound orebody appear to be spatially associated with the Jitou stock, with the highest Cu, S, Au, and Ag being present in proximity of the Jitou stock (Fig. 5A; 803-Geological-Team 1971). The Xinqiao deposit is characterized by metal and ore zonation (Fig. 5B). From the intrusive contact of the Jitou intrusion towards the Carbonaceous strata, the ores are dominated by magnetite, chalcopyrite, pyrite, and Zn-Pb sulfides (Fig. 5B). Mineralization and alteration associations, revealed from bench mapping, core logging and petrographic analysis, are presented in Figures 6-7, with the ore paragenesis summarized in Figure 8.

Skarn assemblages, although volumetrically minor, represent the most intensive alteration at Xinqiao (Fig. 3B, C). The skarn alteration is largely restricted within the contact zone between the Jitou stock and the Permian Qixia Formation limestone (Fig. 3C), but also extends locally into the stratabound orebody distal to the intrusion (Fig. 3B). The skarn alteration typically contains brown to dark-red, anhedral garnet (Fig. 6D), which is commonly overprinted by minor retrograde assemblage, which include actinolite, phlogopite, chlorite, epidote, and tremolite. Wollastonite clusters associated with garnet and diopside assemblages (Fig. 6E) are also developed within the Jitou stock, as a result of hydrothermal metasomatism of carbonate xenoliths (Fig. 3B, C). Epidote also occurs near the intrusive contact zone (Fig. 6F). Late stage euhedral calcite (grain size of ~1-3 cm) occurs in the garnet skarn and are typically enveloped by 1-5 cm wide hematite rings (Fig. 6D). Hydrothermal alteration, largely represented by feldspar dissolution (Fig. 6B) and chlorite formation (Fig. 3G), is extensive throughout the marginal phase of the Jitou stock.

Hydrothermal alteration is relatively weak on both the footwall and hanging walls of the stratabound massive sulfide orebody (803-Geological-Team 1971; Xu and Zhou 2001). However, silicification is variably developed in the sandstones of the Gaolishan Formation, and is generally associated with sericitization whenever silicate clasts are present in the sandstones. The silicification tends to be more intensive close to the stratabound orebody and where sandstones are extensively fractured (Fig. 6O).

Below the stratabound orebody and within the silicificated Gaolishan Formation sandstone, there are numerous planar or wavy quartz vein networks (Gu et al. 2000; Guo et al. 2011), which have been previously interpreted to represent fluid conduits of a submarine exhalative system. The veins comprise subeuhedral-anhedral pyrite grains ranging in size from 0.5to 2 cm and

anhedral fine-grained (<0.3 mm) quartz. In places the vein networks are perpendicular to the stratabound orebody. The pyrite-quartz veins have a sharp contact with the sandstones and lack extensive hydrothermal alteration halos on both sides of the veins except for narrow (commonly <0.5 cm wide) silicification and sericitization selvages.

In the hanging wall of the Qixia Formation limestone, pyrite veins, which are tens of centimetres to meters wide, are locally abundant (Fig. 4). These veins are typically associated with meter-wide marble zones, but no obvious alteration assemblages are documented (803-Geological-Team 1971).

Magnetite is the dominant ore mineral in skarn mineralization, comprising 50-60 vol % of the bulk skarn ore (Fig. 6H). The magnetite ore generally has a massive texture. Although chalcopyrite occurs as centimetre-sized clusters and several millimetre wide veins, it is only sub-economic in the skarn mineralization (803-Geological-Team 1971). Typical pyrite mineralization in the skarn ore occurs as subparallel pyrite veins in quartz dominated matrix with banded textures (Fig. 6I). Skarn hosted pyrite are generally anhedral with a grain size of ~0.3-2 cm associated with anhedral fine-grained (<0.5 cm) quartz.

The stratabound sulfide orebody in the Xinqiao deposit is dominated by massive pyrite ore (Fig. 6J-L), although massive chalcopyrite and sphalerite veins are also present (Fig. 6M-N). Three types of pyrite have been identified (py1, py2 and py3). In addition, previous studies document pentagonal, dodecahedron and fine-grained anhedral pyrite (Zhou et al. 2010; Xiao et al. 2016). Type 1 pyrite (py1) is the most abundant and consists of anhedral grains with micro-fractures (Fig. 6J, 7B). It typically occurs without associated minerals, with rare exceptions where quartz and chalcopyrite veinlets are observed. Type 2 pyrite is euhedral with a cubic form, and typically occurs as clusters with a grain size of 0.3-2.5 cm (Fig. 6K, 7A), and is not

associated with other minerals. Type 3 is featured by massive colloform texture (Fig. 6L). The colloform pyrite has zoned texture (Fig. 7C) with individual grains ranging from 0.5 to 2 μm size (Zhou et al. 2010; Xie et al. 2014; Xiao et al. 2016). In places, the colloform pyrite includes silver-yellow anhedral pyrite clusters, and is cut by ~0.5 cm wide silver-yellow pyrite veins (Fig. 6L).

Massive chalcopyrite is also present in the stratabound orebody. Chalcopyrite ore typically has a green-yellow colour with massive texture and is predominately comprised of chalcopyrite (Fig. 6M). Sphalerite occurs as 5-10 cm wide veins in the Qixia Formation limestone, with associated calcite and pyrite (Fig. 6N). In addition, sphalerite is also present as solid solution in chalcopyrite (803-Geological-Team 1971).

Samples and Analytical methods

Samples

Two diopside-bearing samples (XQ7 and XQ10; Fig. 6E) were collected from the contact zone (Fig. 3B) between the Jitou stock and the Qixia Formation dolomitic limestone in the open pit. Two quartz bearing banded pyrite-quartz vein (Fig. 6I) samples (XQ82 and XQ86) were collected from the same position. A further two quartz bearing samples (XQ8-1 and XQ8-2) were collected from the Gaolishan Formation sandstone hosting quartz-pyrite vein networks (Fig. 6O) at the north wall of the open pit (Fig. 3B). Diopside and quartz bearing assemblages from these samples were selected for fluid inclusion study.

Samples (XQ5-1, 5-2 and 5-3) used for SIMS oxygen isotope analysis also were collected from the contact zone (Fig. 3B) between the Jitou stock and the Qixia Formation dolomitic limestone in the open pit. These samples are dominated by anhedral garnet overprinted with

calcite (Fig. 6D) and anhedral quartz interstitial to the garnet grains (Fig. 7E). Four quartz-pyrite veins (XQ8-3, 8-4, 8-5 and 8-6) hosted in the Gaolishan Formation sandstone were collected from the same position as XQ8-1 and 8-2.

One diorite porphyry sample (XQ09-3) was collected from the marginal phase of the Jitou stock (Fig. 3B), and comprises plagioclase (27 vol. %) and hornblende (23 vol. %) as phenocrysts, with a groundmass of plagioclase, quartz and hornblende, and accessory minerals of apatite, titanite, zircon and magnetite. The sample possesses extensive plagioclase phenocryst dissolution indicating intensive hydrothermal alteration (Fig. 6B). The XQ1 sample was collected from south wall of the open pit (Fig. 3B), which is diorite porphyry in composition. This unit has a similar mineralogy to the marginal phase of the Jitou stock, but possesses less abundant phenocrysts and is free of alteration (Fig. 6C). Zircon grains were separated from these two samples for SIMS U-Pb geochronology.

Four massive pyrite samples were collected from the main stratabound massive sulfide orebody at the bottom northeast corner of the open pit for Re-Os geochronology study. Samples XQ15 and XQ24 are dominated by py1 (Fig. 6J, 7B), whereas samples XQ25 and XQ10 are mainly composed of py2 (Fig. 6K, 7A)..

Microthermometry

Microthermometric analysis of fluid inclusions in diopside and quartz was carried out at the fluid inclusion laboratory at the Faculty of Earth Resources, China University of Geosciences, Wuhan, using a Linkam THMS600 heating and freezing stage mounted on an Olympus transmission light microscope. Synthetic fluid inclusion standards (pure CO_2 and pure water) were used at -56.6, 0, 10.2, and 374°C to assess the accuracy of the stage (Baumgartner et al.

2014). Analytical uncertainties are better than ±0.2 °C and ± 1 °C for measurements below and above 31.1 °C (critical point of CO_2), respectively. The volumetric fraction of liquid or vapor phases present in fluid inclusions was estimated at room temperature with reference to the volumetric chart of Roedder (1984). Bulk salinity was calculated from the final ice melting temperature, or halite dissolution temperature (Bodnar and Vityk 1994) for hypersaline fluid inclusions.

SIMS oxygen isotope analysis

Quartz oxygen isotope analysis was carried out at the Institute of Geology and Geophysics, Chinese Academy of Sciences with a CAMECA IMS-1280 SIMS. Sample preparation and instrument operation conditions are the same as Li et al. (2010a) and are briefly summarized here. Quartz bearing assemblages were mounted with NBS-28 (Matsuhisa 1974) and Qinghu quartz standards and then polished and coated with gold. The Cs^+ primary ion beam was accelerated at 10 kV, with a beam intensity of ca. 2 nA and rastered over a 10 μm area. The spot size as an ellipse was about 10 × 20 μm in diameter. Oxygen isotopes were measured using multi-collection mode on two off-axis Faraday cups. The intensity of ^{16}O ion was typically 10^9 cps during this study. The instrumental mass fractionation factor (IMF) was corrected using NBS-28 with a $\delta^{18}O$ value of 9.5 ‰ (V-SMOW, same as below; Matsuhisa 1974). Measured $^{18}O/^{16}O$ ratios were normalized by using V-SMOW compositions ($^{18}O/^{16}O$ = 0.0020052), and then corrected for the IMF. Uncertainties on individual analysis were usually better than 0.3 ‰ (2 SE). All measurements were bracketed by or interspersed with analyses of Qinghu quartz that served as an in-house standards. Our measurements of Qinghu quartz showed small amounts of random drift through time (in all cases <0.6 ‰). The weighted mean of 41 measurements is 8.66 ± 0.05 ‰

(95 % conf., Table A1, Fig. A1, 2 SD = 0.28), which is identical, within uncertainty, to the recommended value (8.6 ± 0.2 ‰; 2 SD, Li Xian-Hua, unpublished). The data are reported in Table 1 and graphically presented in Fig.10. The weighted mean $\delta^{18}O$ value of each sample was calculated by *Isoplot 3.0* with rejection of any data outside of the 2 sigma uncertainty (Ludwig 2003).

SIMS zircon U-Pb dating

Zircon U-Pb dating was conducted at the Institute of Geology and Geophysics, Chinese Academy of Sciences with a CAMECA IMS-1280HR SIMS. Sample preparation and instrument operation conditions are the same as previous studies (Li et al. 2009; Li et al. 2010a) and are briefly summarized here.

Zircon grains were mounted with geochronology standards (Plešovice and Qinghu zircon) (Sláma et al. 2008; Li et al. 2013) and then polished and coated with gold. During U-Pb analysis, zircon grains were sputtered by an O^{2-} primary ion beam with a beam intensity of ca. 8 nA and a beam diameter of 20 μm. An ellipsoidal spot approximately 20 × 30 μm in size was created at the sample surface as the ion beam was at an angle with the sample surface. U-Pb concentration and isotopic compositions were calibrated against the Plešovice zircon standard with a recommended age of 337.13 ± 0.37 Ma (Sláma et al. 2008). Common Pb was corrected using measured non-radiogenic ^{204}Pb and an average present day crustal Pb isotopic composition defined by Stacey and Kramers (1975). The Wetherill concordia plots and derived concordia ages were calculated by using *Isoplot* v.3.0 (Ludwig 2003). As a monitor of data quality, the Qinghu zircon standard was analysed between samples. Seven analyses of Qinghu zircon during this study (Table A2, Fig. A2) yielded a weighted mean $^{206}Pb/^{238}U$ age of 160.1 ± 1.8 Ma at 95 % confidence (MSWD

= 0.43), which is in agreement with the reported reference value of 159.5 ± 0.2 Ma (Li et al. 2013). The U-Pb data are reported in Table 2, and illustrated in Wetherill concordia plots and weighted average of $^{206}Pb/^{238}U$ ages (Fig.11).

Pyrite Re-Os dating

Massive pyrite samples were crushed to 20-30 mesh and then handpicked under a microscope, the estimated pyrite purity is better than 98 %. The pyrite Re-Os analytical method was the same as documented by Selby et al. (2009) and is briefly outlined here. Purified pyrite aliquots were accurately weighted and loaded into carius tubes with known amounts of mixed Re-Os tracer solution containing ^{185}Re and ^{190}Os. The carius tubes were then sealed, digested and equilibrated using a mix of 11 N HCl (3 ml) and 15.5 N HNO_3 (8 ml) at 220 ^{o}C for 48 hours. Osmium was isolated and purified from the acidic digestion medium using solvent ($CHCl_3$) and microdistillation methods, and rhenium was separated by solvent extraction (acetone) and anion chromatography (Selby and Creaser 2001). The purified Re and Os were loaded onto Ni and Pt filaments, respectively, with the isotopic measurements conducted using negative thermal ionization mass spectrometry (Creaser et al. 1991) on a Thermo Electron TRITON mass spectrometer. The Os data was collected via ion counting using a secondary electron multiplier in peak-hopping mode, and Re data was collected with static Faraday collectors. Total procedural blanks were monitored during the course of study. Blanks for Re and Os were 2.8 ± 0.6 and 1.7 ± 2.0 pg, respectively, with an average $^{187}Os/^{188}Os$ value of 0.19 ± 0.10 (2σ, n = 3). The presented uncertainties include the fully propagated uncertainties in Re and Os isotopic compositions measurements, blank abundances and isotopic compositions, spike calibrations and

reproducibility of standard Re and Os isotope values. Decay constant uncertainties are not propagated as the uncertainty of Re-Os is dominated by analytical uncertainty.

Results

Fluid inclusion

Fluid inclusions were classified as primary, pseudosecondary and secondary inclusions following the definition of Goldstein and Reynolds (1994). Both primary and pseudosecondary fluid inclusions homogenised to liquid followed by dissolution of halite whenever it is present. No clathrate formation was recorded in this study. However, a few fluid inclusions hosted in diopside, 6 of them did not homogenize despite heating to ~598 ^{o}C for ~10 minutes.

Diopside predominately hosts liquid-vapor two-phase fluid inclusions with a few containing halite as daughter minerals. These fluid inclusions are generally round and vary in size from 5 to 12 μm (Fig. 9A&B). Vapor phase accounts for 30 and 60 vol. % of individual fluid inclusions. Thirty-nine measurements yield variable homogenization temperatures and calculated salinities (Fig. 10). The two-phase aqueous fluid inclusions (n = 28) yielded homogenization temperatures of 450-~600 ^{o}C and calculated salinities of 13-21 wt. % NaCl equiv. The halite bearing inclusions (n = 11) yield homogenization temperatures of 450 to ~600 ^{o}C and salinities of 35-58 wt. % NaCl equiv. calculated from halite melting temperature

Quartz from the banded quartz-pyrite veins in the skarn ores hosts abundant two-phase aqueous fluid inclusions, which are round to sub-round or polygonal in shape, range in size from a few to >10 μm, and contain 20-50 vol. % vapor phase (Fig. 9C). Homogenization temperatures and calculated salinities for these fluid inclusions (n = 29) are 290-360 ^{o}C (average = 328 ± 46 $^{\circ}$C), and 5-12 wt. % NaCl equiv, respectively (Fig. 10).

Quartz from the quartz-pyrite vein networks in the Gaolishan Formation sandstone host liquid-rich aqueous fluid inclusions that are elongated with a diameter of ~10 μm and contain <35 vol. % vapor. The inclusions (n = 46) yielded homogenization temperatures between 200 and 300 ºC (average = 258 ± 42 ˚C), and calculated salinities of 2-10 wt. % NaCl equiv. (Fig. 10).

Oxygen isotopes

In total, 32 and 71 *in-situ* quartz oxygen isotope analyses were conducted for quartz from the banded skarn ore (Fig. 6I, 7E) and quartz-pyrite veins in the Gaolishan Formation sandstone (Fig. 6O, 7F), respectively. Mineral inclusions are rare in these anhedral quartz grains except pyrite in some cases (Fig. 7E-F). The analysed quartz grains exhibit no cathodoluminescence, indicating homogeneous texture and composition. The data are reported in Table 1 and graphically presented in Figure 11.

Quartz grains from the skarn ore samples yield $\delta^{18}O$ values of 11.09 to 13.79 ‰ (2 SD; n = 22). No systematic variation in the $\delta^{18}O$ values were observed between samples. Quartz from quartz-pyrite vein networks in the Gaolishan Formation sandstone yield $\delta^{18}O$ values predominately between 13.47 and 17.76 ‰, with a mean of 15.57 ± 1.92 (2 SD, n = 60). Again, no systematic $\delta^{18}O$ values variations were observed among the analysed samples.

Zircon U-Pb ages

All zircon grains recovered from the marginal phase of the Jitou stock and the alteration-free diorite porphyry dike are pale, euhedral and prismatic, and their CL images revealed well-developed oscillatory zonation (Fig. 12). The morphological and textural features confirm a magmatic origin for the zircon grains investigated. The U-Pb data are summarized in Table 2 and

illustrated in Figure 12. For the marginal phase diorite porphyry of the Jitou stock, 16 analyses yield a Wetherill concordia age of 138.5 ± 1.0 Ma (95 % conf., MSWD = 0.6), which is identical to the weighted mean $^{206}Pb/^{238}U$ age (138.5 ± 1.0 Ma, 95 % conf., MSWD = 0.24). For the diorite porphyry dike, 22 analyses showed limited scatter and yield a Wetherill concordia age of 130.6 ± 1.1 Ma (95 % conf., MSWD = 0.1), and an identical weighted average of $^{206}Pb/^{238}U$ age of 130.7 ± 0.9 Ma (95 % conf., MSWD = 1.1).

Pyrite Re-Os geochronology

The Re-Os data for pyrite samples from the stratabound orebody are reported in Table 3 and graphically shown in Figure 13. Three of the four pyrite samples possess Re concentrations of 26 to 31.9 ppb, with the remaining one containing 1.1 ppb Re. The total Os concentrations range from 31 to 124.7 ppt. With the exception of the relatively low Re sample, the sample set has elevated $^{187}Re/^{188}Os$ (~2400 to 15000) and $^{187}Os/^{188}Os$ (~7.6 to 39) values. The Re-Os data for all samples possess high error correlation (*rho*) values (>0.92). These features characterise samples XQ10, 24 and 25 as low-level highly radiogenic sulphides, which means that the bulk Os, especially ^{187}Os predominately consists of radiogenic ^{187}Os ($^{187}Os^{r}$), rather than common Os that was incorporated into the pyrite during its formation (i.e., common Os) (Stein et al. 2000; Selby et al. 2009). Including the error correlation value, *Isoplot* cannot solve a best fit for the Re-Os data of the pyrite samples. This is, in part, due to associated uncertainty of the $^{187}Re/^{188}Os$ and $^{187}Os/^{188}Os$ values (~2.3 to 12%), and the *rho* values (>0.92), which are calculated from the $^{187}Re/^{188}Os$, $^{187}Os/^{188}Os$, and $^{187}Re/^{187}Os$ values and their uncertainties (Cumming et al. 1972). Not including the *rho* value *Isoplot* calculates a Model 3 (assumes that the scatter about the degree of fit is the result of the assigned uncertainties and an unknown, but normally distributed

variation in the initial $^{187}Os/^{188}Os$ values) date for the Re-Os data of 142 ± 47 Ma, with an initial $^{187}Os/^{188}Os$ value of 1.2 ± 3.5 (MSWD = 7.8).

Discussion

Nature and origin of ore-forming fluids

Fluid inclusions in diopside from the uneconomic skarn exhibit high homogenization temperatures (450-600 °C) with high, but variable salinities (13-58 wt. % NaCl equiv., Fig. 10), features commonly cited as evidence for magmatic hydrothermal fluids (Meinert et al. 2003). The high and low salinity fluid inclusions in diopside have similar homogenization temperatures (Fig. 10), potentially indicating fluid unmixing during the skarn formation. Similar observations have been made for garnet and diopside in skarn mineral deposits elsewhere (Xiao et al. 2002; Meinert et al. 2005; Bodnar et al. 2014). Field relations indicate that this magmatic hydrothermal fluid was most likely sourced from the Jitou stock and/or the underlying magma chamber. The banded quartz-pyrite veins (Fig. 6I) are paragenetically coeval or slightly postdate retrograde alteration assemblages (Fig. 8). Fluid inclusions hosted by quartz grains from the veins have moderate homogenization temperatures (290-360 °) and moderate to low salinities (5-12 wt. % NaCl equiv.; Fig. 10), comparable to those documented in retrograde alteration assemblages of skarn deposits (Meinert et al. 1997; Xiao et al. 2002; Meinert et al. 2005; Bodnar et al. 2014).

Fluid inclusions hosted by quartz grains from quartz-sulfide veinlets beneath the stratabound massive sulfide ore possess moderate-low homogenization temperatures (200-300 °C) and salinities (2-10 wt. % NaCl equiv.; Fig. 10), which are slightly lower than those in banded quartz of the skarn ore, but are comparable with the fluids associated with the retrograde alteration assemblages in typical skarn deposits (Bodnar et al. 2014). Moreover, these fluid inclusion

characteristics are in sharp contrast to those documented in typical SEDEX deposits (Nesbitt et al. 1984; Leach et al. 2004). For example, in Red Dog deposit, fluid inclusions hosted by quartz have significant lower homogenization temperatures and salinities (typically < 230 °C and 5 wt. % NaCl equiv; Leach et al. 2004). The homogenization temperatures obtained in this study represent a minimum estimate for temperatures of the ore-forming fluids, the values, however, are obviously higher than homogenization temperatures of fluid inclusions from typical SEDEX deposits (Leach et al., 2005) and measurements for modern Zn and Pb rich sedimentary brines (60-160 °C), which are believed to be the modern analogues of SEDEX ore-forming fluids (Cooke et al. 2000).

Based on the average homogenization temperatures (Fig. 10), the calculated $\delta^{18}O$ values of fluids associated with quartz from the banded skarn ore (328 ± 46 °C) and quartz-pyrite veins (258 ± 42 °C) hosted in sandstone are 6.22 ± 1.59 ‰ and 6.81 ± 2.76 ‰, respectively (Fig. 11). These values confirm a magmatic origin for the ore-forming fluids and that both types of mineralization may have precipitated from the same fluid system. Alteration assemblages in conduit pipes beneath stratabound orebody in classic SEDEX deposits are expected to record a mixing fluid between deep circulated hydrothermal fluid and seawater (Davies et al. 1990; Jiang et al. 1998; Cooke et al. 2000; Slack et al. 2015). Oxygen isotope compositions of carbonates (dolomite, kutnohorite, manganosiderite and calcite) suggests that the fluids responsible for SEDEX Pb-Zn mineralization at the vent site of Sudbury Basin have $\delta^{18}O$ values of ~-1 ‰ (Davies et al. 1990). In contrast, the quartz-pyrite vein networks hosted by the Gaolishan Formation sandstone have oxygen isotopes that are significantly heavier than the fluid typical of SEDEX systems, arguing against a SEDEX fluid origin.

In summary, fluid inclusions in quartz from banded skarn ore and pyrite-quartz veins hosted in Gaolishan Formation sandstone, the latter having long been considered to be a product of SEDEX mineralization (Gu et al. 2000; Gu et al. 2007; Guo et al. 2011), have broadly comparable homogenization temperatures, calculated salinities, and $\delta^{18}O$ values. The values are also comparable to those documented in retrograde alteration assemblages from typical skarn deposits, both locally in Tongling area (Xiao et al. 2002; Wang and Ni 2009) and globally (Meinert et al. 2005; Bodnar et al. 2014). In contrast, these features are distinctly different from those observed in typical SEDEX deposits and their modern analogues (Davies et al. 1990; Jiang et al. 1998; Cooke et al. 2000; Slack et al. 2015). Taken together, we favour a magmatic origin for the fluid associated with the quartz-pyrite veins at Xinqiao.

Timing of mineralization

The SIMS zircon U-Pb data (Fig. 12) suggest that the marginal phase of the Jitou stock (Fig. 6B) crystallized at 138.5 ±1.1 Ma, whereas the quartz diorite (Fig. 6C) was emplaced at 130.6 ±1.1 Ma. The present SIMS zircon U-Pb age (138.5 ±1.1 Ma) of the Jitou stock is younger than a previous SHRIMP zircon U-Pb age (146.4 ± 4.3 Ma; Wu et al. (2009), but is within analytical uncertainty of an earlier SHRIMP zircon age (140.4 ± 2.2 Ma; Wang et al. (2004). The samples dated by Wu et al. (2009) and Wang et al. (2004) were monzonite and quartz diorite from the Jitou stock, which exhibit intensive propylitic alteration as observed in this study. Although there are textural variations across the Jitou stock, no crosscutting relationships has been observed between the central and marginal phases. As a result, the textural and compositional changes across the pluton is assumed to be controlled by cooling and fractional crystallization. In this case, a multi-stage intrusive history is not favored. Further, a prolonged crystallization history is

excluded considering the small volume of the Jitou stock (Fig. 3A-B) and thermal modeling results that suggest a single intrusive event with a size of 160 km^3 can only sustain hydrothermal circulation and near-surface geothermal activity for approximately 800,000 years (Cathles et al. 1997). Consequently, the difference between the two SHRIMP zircon U-Pb ages (Wang et al. 2004; Wu et al. 2009) and the new SIMS data is most likely caused by bias between labs and methods as demonstrated by Li et al. (2015), although contamination from inheritance cannot be precluded (Mezger and Krogstad 1997; Schoene 2014). Based on the discussion above, our SIMS U-Pb age is considered as the best estimate for the crystallization timing of Jitou stock (Fig. 12A). The alteration-free diorite porphyry dike is ~8 Ma younger than the Jitou stock, indicating a magmatic activity after the emplacement of the Jitou stock.

The Re-Os data (not including the *rho* values) of the 4 massive pyrite samples from the stratabound orebody yield a Model 3 Re-Os date of 142 ± 47 Ma (initial $^{187}Os/^{188}Os$ = 1.2 ± 3.5, Fig. 13). The degree of scatter (MWSD = 7.8) about the best fit line of the Re-Os data is beyond that that can be solely explained by analytical uncertainties (Wendt and Carl 1991). The possible reasons to account for the scatter are: (1) open system behavior of Re-Os isotopic system in these pyrite samples (Nakai et al. 1993); (2) multiple pyrite generations in multiple mineralization events (different t, typically different initial $^{187}Os/^{188}Os$ values); (3) prolonged mineralization duration from a single fluid sources (different t, similar $^{187}Os/^{188}Os$ values) (Hnatyshin et al. 2015); and (4) simultaneously mineralization from multiple sources fluid (same t, different $^{187}Os/^{188}Os$ values) (Ostendorf et al. 2015).

With the exception of sample XQ15, none of Re-Os data for pyrite of this study fall along a ~320 Ma reference line (Fig. 13). Sample XQ15 yields a positive initial $^{187}Os/^{188}Os$ value (0.5) at 320 Ma (Table 3). The remaining samples (XQ10, 24 and 25) yield significant negative initial

$^{187}Os/^{188}Os$ values (-5.4 to -40.6) at 320 Ma (Table 3), which would suggest that if these samples were formed at ~320 Ma the Re-Os systematics have been significantly disturbed/reset.

Further, if we consider samples XQ10, 24, 25 only, the Re-Os data yield a highly imprecise Model 3 data (153 ±160 Ma; Fig. 13) with an initial $^{187}Os/^{188}Os$ value of 0 ± 26 (MWSD = 151). The decrease in precision of the Re-Os data is likely caused by the removal of sample XQ15, which given its low $^{187}Re/^{188}Os$ and $^{187}Os/^{188}Os$ values relative to samples XQ10, 24, 25, may have aided in anchoring the regression line. Additionally, the low precision in the Re-Os data is likely due to highly variable initial $^{187}Os/^{188}Os$ values. Based on above discussion, the variability in the initial$^{187}Os/^{188}Os$ values could be explained by the penecontemporaneous formation of the sulfides from fluids with different $^{187}Os/^{188}Os$ values, and/or inheritance of $^{187}Os/^{188}Os$ values from the country rock through fluid-rock interactions, and/or incomplete resetting of the Re-Os systematics of older pyrite. In addition, Os out of equilibrium in massive pyrite sample due to Os isotopes exchange by solid-state diffusion in pyrite (Brenan et al. 2000) can also account for the scatter observed in this study.

Although the Re-Os data yield a poorly-defined best fit line, the Re-Os data of the pyrite samples yield a date that, including uncertainty, overlaps with the age of the Jitou stock (Fig. 12A). In addition, this age, within uncertainty, agrees with the 112.6 ± 7.8 Ma pyrite Rb-Sr and the 126 ± 11 Ma pyrite Re-Os mineralization age with samples collected from the stratabound orebody (Wang et al. 2005; Xie et al. 2009), and a recently published quartz fluid inclusion Rb-Sr date representing the age of quartz-pyrite veins hosted by sandstone is 138± 2.3 Ma (Zhang et al. 2015).

However, all these early Cretaceous mineralization ages are significantly younger than the 319 ± 13 Ma (MSWD = 16) pyrite Re-Os data representing the "age" of pyrite-quartz veinlets

hosted by sandstone beneath the stratabound orebody (Guo et al. 2011). The samples of Guo et al. (2011) were collected frompyrite-quartz vein networks hosted by Gaolishan Formation sandstone described in this study (Fig. 6O) and Zhang et al. (2015). But both previous (Wang and Ni 2009) and this study report fluid inclusions data, that is indicative of a magmatic origin. This magmatic origin is most likely related with the Jitou stock, as supported by the 138 ± 2.3 Ma quartz fluid Rb-Sr (Zhang et al. 2015), which is identical to the emplacement age of the Jitou stock (Fig. 12).

As discussed above, the mineralization of the stratabound orebody and the quartz-pyrite veins hosted by sandstone is, at least in part, associated with a Cretaceous hydrothermal event, likely genetically related to the Jitou stock, as confirmed by the fluid inclusion and oxygen isotope data. However, the age presented here has large uncertainties, and the quartz fluid inclusion Rb-Sr system has uncertainties related to multiple generations of fluid inclusions. This proposes the requirement for additional accurate and precise geochronology to better constrain the mineralization age, and thus the genesis and ore-forming processes of Xinqiao.

A Cretaceous carbonate replacement deposit

As discussed above, the nature of ore-forming fluids and mineralisation ages invoke for a Cretaceous magmatic origin for the Xinqiao deposit, presumably genetically related to the Cretaceous Jitou stock and potential associated intrusions at depth. This magmatic model for the Xinqiao deposit is further supported by several lines of evidence. (1) The close spatial association between the Cretaceous intrusions and the stratabound massive sulfide orebody (Fig. 3A-C), and the zoned metal distribution grading from magnetite through chalcopyrite to auriferous pyrite and then Zn-Pb sulfides well correlated with distance from the Jitou stock (Fig.

5A, B). (2). Coarse grained pyrite (Fig. 6K, 7A) is common in the stratabound orebody at Xinqiao, which contrasts to the fine grained nature of pyrite typically occurring in SEDEX deposits (Leach et al. 2005). The locally presented massive, colloform and laminated ore textures (Fig. 6J-L, 7B-C) at Xinqiao are not diagnostic of SEDEX deposits as they are also widely present in skarn deposits (Meinert 1982; Sato 1984). (3) The quartz-pyrite vein networks hosted by Gaolishan Formation sandstone are locally broadly perpendicular to the stratabound orebody, but are controlled by brittle fractures (803-Geological-Team 1971; Pan and Dong 1999; Gu et al. 2000; Guo et al. 2011). This contrasts to synsedimentary faults that are characteristic of many SEDEX deposits (Large 1983; Goodfellow et al. 1993). (4) The pyrite-quartz networks in the Gaolishan Formation sandstone lack zoned alteration halos (Wang and Ni 2009; Guo et al. 2011; Zhang et al. 2015) and are predominately comprised of coarse grained Au-enriched pyrite (Fig. 6O, 7A). This is different from typical feeder zones of SEDEX deposit, e.g., Sullivan Pb-Zn deposit in British Columbia and Pomorzany Pb-Zn deposit in Poland, where the fluid conduits have zoned geometries with the sulphides exhibiting fine-grained colloform textures, with abundant quartz, tourmaline and Fe-Mn carbonates alteration assemblages, and the sulfides are rarely rich in Au (Jiang et al. 1998; Leach et al. 2005).

In summary, ore-forming fluids at Xinqiao have similar temperatures, salinities and $\delta^{18}O$ values with those observed in typical skarn deposits, but are distinctly different from those documented in SEDEX deposits and their modern analogues. The close association of the mineralization with magmatism, metal zoning, ore distribution patterns and fluid nature all show a magmatic affinity. The field occurrences coupled with geochemical and geochronological data suggest that the Xinqiao deposit can be best classified as a carbonate replacement deposit associated with early Cretaceous magmatism.

General patterns of stratabound massive ore deposits and implications for exploration

Extensive sulfur isotope studies have been conducted in an attempt to constrain the genesis of stratabound massive sulfide deposits along MLYMB. As presented in Figure 14 stratabound massive sulfide deposits have pyrite $\delta^{34}S$ values ranging from -1.1 to 7.7 ‰ with an average of 3.8 ‰ (n = 128), with exception of three analyses (-9, -13, 11 ‰, Zhou et al. 1983; Zhou 1984; Zhao et al. 1985; Liu and Liu 1991; Pan and Dong 1999; Xu et al. 2004; Li 2006; Xu et al. 2010). The sulfur isotope data are comparable with those of Cretaceous intrusions and associated skarn and porphyry deposits, which show limited variations between -1.3 and 7.0 ‰, with a mean of 2.8 ‰ (n = 56, Pan and Dong 1999; Xu et al. 2010). In contrast, the diagenetic pyrite samples from the major host rocks of the stratabound massive sulfide deposits, Carboniferous carbonates, have negative $\delta^{34}S$ values with significant fluctuations between -35.4 and -17.6 ‰ (n = 10, Zhou 1984; Xu et al. 2010). Thus, pyrite sulfur isotope data suggest that the stratabound massive sulfide deposits are most likely related to the spatially associated Cretaceous magmatic systems, and have limited contribution from sedimentary sulfur.

Mineralization age is the most critical information to understand the genesis of stratabound massive sulfide deposits in MLYMB. As summarized in Table 3 and Figure 15, both Carboniferous and Cretaceous ages are reported. Although the magmatic rocks and associated porphyry-skarn deposits were broadly formed between 148 and 130 Ma, the reported mineralization ages of stratabound massive sulfide deposits derived from pyrite Rb-Sr and pyrite Re-Os predominately are based on Xinqiao and show significant scatter (Fig. 15; (Meng et al. 2004; Wang et al. 2005; Xie et al. 2009; Guo et al. 2011; Zhang et al. 2015). As discussed earlier, there is a need for further accurate and precise ages.

Geochemical anomaly mapping is one the most important guidance for mineral exploration. Soil Cu, Pb, Zn, Au and Ag geochemical anomaly map in the Tongling area (Fig. 16, Jiujiang conference communication, 2010) shows a strong concentric zonation around Miocene intrusions, which are the same as documented in Mankayan intrusion-centered Cu-Au district, Philippines (Chang et al. 2011). This is different to the geochemical anomalies around SEDEX deposits, which are stratigraphically controlled, as demonstrated by Lambert and Scott (1973) in the HYC deposit, Australia, where Mn and to lesser extent Pb and Zn, occur in dolomites in a narrow envelope surrounding the stratabound orebody, and extends along the favourable horizon at the base of pyrite shale member for at least 23 km.

Given the close spatial association between the stratabound massive sulfide deposits and Cretaceous magmatism, magmatic affinity of the alteration assemblages and geochemical data, as well as the structural/unconformity controlled position of the ore body, we propose that a promising exploration target for stratabound massive sulfide deposits is the convergence zone where the Cretaceous intrusions intrude or overprint the unconformity between the Late Devonian Wutong and the Early Carboniferous Gaolishan Formations. Early Cretaceous intrusions with known associated stratabound massive sulfide deposits may also contain Cu (Mo and Au) resources at depth as porphyry/skarn mineralization, as supported by the newly discovered porphyry Cu-Mo deposit at depth of Dongguashan stratabound massive sulfide deposit (Yuan et al. 2014).

Conclusions

Fluid inclusions hosted by prograde diopside yield homogenization temperatures between 450-600 ^{o}C and calculated salinities of 13-58 wt. % NaCl equiv. While fluid inclusions hosted by

quartz from the banded skarn ore and pyrite-quartz vein networks in the Gaolishan Formation sandstone have homogenization temperatures of 290-360 and 200-300 ºC, with calculated salinities of 5-12 and 2-10 wt. % NaCl equiv respectively. Quartz grains from the banded skarn ore and the pyrite-quartz vein networks hosted by Gaolishan Formation sandstone have SIMS $\delta^{18}O$ values of 12.32 ± 0.55 (2 SD, n = 22) and 15.57 ± 1.92 ‰ (2 SD, n = 60), with calculated fluid $\delta^{18}O$ values of 6.22 ± 1.59 and 6.81 ± 2.76 ‰ based on the average fluid inclusion homogenization temperatures of 328 ± 46 and 258 ± 42 ºC of this study, respectively. The SIMS zircon U-Pb data indicate the Jitou stocks was emplaced at 138.5 ±1.1 Ma (2σ, MSWD = 0.6), and the alteration-free diorite porphyry dike was crystalized at 130.6 ±1.1 Ma (2σ, MSWD = 0.1). Massive pyrite ore samples from the stratabound orebody yield a 142 ± 47 Ma Model 3 age. All the fluid inclusion, oxygen isotope and geochronology data support a magmatic origin, together with the magmatic affinity of the orebody and alteration assemblages with Jitou stock, we classify the Xinqiao deposit as a Carbonate replacement deposit genetic related with the Jitou stock.

The spatial association of stratabound massive sulfide orebodies along MLYMB with Cretaceous magmatism, pyrite sulfur isotope and zoned geochemical anomalies all can be explained neatly by a magmatic genetic scenario, although further accurate and precise mineralization dating is needed for further understanding the ore-forming process. The association between stratabound ores with Early Cretaceous magmatism has broad implications for future mineral exploration, with emphasis on conjunction between Cretaceous magmatic intrusions and Early Carboniferous carbonates, particularly around Cretaceous intrusions with associated skarn and porphyry mineralization. Additionally, our model may imply that porphyry

and skarn Cu-Au systems could occur beneath the known stratabound massive sulfide ore deposits in this region.

Acknowledgements

Hao Hu and Sha-Sha Liu assisted with the fieldwork. Hong-Xia Ma, Jiao Li and Xiao-Yan Jiang, Yu Liu, Guo-Qiang Tang are acknowledged for generous help during SIMS U-Pb and SIMS O isotope analysis. This research is jointly supported by the National Natural Science Foundation of China (41325007, 91414301), the National Basic Research Program of China (2012CB416802), and the Nanjing Centre of China Geological Survey. DS acknowledges the support of the TOTAL endowment fund. Comments from Zhao-Shan Chang, Peter Megaw and an anonymous reviewer on an earlier version of this work are acknowledged. Two anonymous reviewers for OGR are also thanked for further improvements of this paper.

References

803-Geological-Team (1971) Reserves report of Xinqiao Cu bearing pyrite deposits, Tonglong, Anhui. Metallurgical Geology Bureau of Anhui Province, pp 141. (In Chinese).

Baumgartner M, Bakker RJ, Doppler G (2014) Re-equilibration of natural H_2O-CO_2-salt-rich fluid inclusions in quartz-Part 1: experiments in pure water at constant pressures and differential pressures at 600 ^{o}C. Contributions to Mineralogy and Petrology 168:1-14. doi: doi:10.1007/S00410-014-1017-3.

Bodnar RJ, Vityk MO (1994) Interpretation of microthermometric data for H_2O-NaCl fluid inclusions In: Vivo BD, Frezzotti ML (eds) Fluid inclusions in minerals: Methods and applications. Virginia Tech, Blacksburg, VA, pp 117-130.

Bodnar RJ, Lecumberri-Sanchez P, Moncada D, Steele-MacInnis M (2014) 13.5 - Fluid Inclusions in Hydrothermal Ore Deposits In: Turekian HDHK (ed) Treatise on Geochemistry (Second Edition). Elsevier, Oxford, pp 119-142.

Brenan JM, Cherniak DJ, Rose LA (2000) Diffusion of osmium in pyrrhotite and pyrite: implications for closure of the Re-Os isotopic system. Earth and Planetary Science Letters 180:399-413. doi: doi:10.1016/S0012-821x(00)00165-5.

Cathles LM, Erendi AHJ, Barrie T (1997) How long can a hydrothermal system be sustained by a single intrusive event? Economic Geology 92:766-771. doi: 10.2113/gsecongeo.92.7-8.766.

Chang ZS, Hedenquist JW, White NC, Cooke DR, Roach M, Deyell CL, Garcia J, Gemmell JB, McKnight S, Cuison AL (2011) Exploration Tools for Linked Porphyry and Epithermal Deposits: Example from the Mankayan Intrusion-Centered Cu-Au District, Luzon, Philippines. Economic Geology 106:1365-1398. doi: 10.2113/econgeo.106.8.1365.

Cooke DR, Bull SW, Large RR, McGoldrick PJ (2000) The importance of oxidized brines for the formation of Australian proterozoic stratiform sediment-hosted Pb-Zn (sedex) deposits. Economic Geology and the Bulletin of the Society of Economic Geologists 95:1-17.

Creaser RA, Papanastassiou DA, Wasserburg GJ (1991) Negative Thermal Ion Mass-Spectrometry of Osmium, Rhenium, and Iridium. Geochimica Et Cosmochimica Acta 55:397-401. doi: 10.1016/0016-7037(91)90427-7.

Cumming G, Rollett J, Rossotti F, Whewell R (1972) Statistical methods for the computation of stability constants. Part I. Straight-line fitting of points with correlated errors. Journal of the Chemical Society, Dalton Transactions:2652-2658.

Davies JF, Leroux MV, Whitehead RE, Goodfellow WD (1990) Oxygen-Isotope Composition and Temperature of Fluids Involved in Deposition of Proterozoic Sedex Deposits, Sudbury Basin, Ontario. Canadian Journal of Earth Sciences 27:1299-1303. doi: 10.1139/e90-139.

Ding X, Jiang S-Y, Ni P, Gu L-X, Jiang Y-H (2005) Zircon SIMS U–Pb geochronology of host granitoids in Wushan and Yongping copper deposits, Jiangxi Province. Geological Journal of China Universities 11:383-389.

Goldstein RH, Reynolds TJ (1994) Systematics of fluid inclusions in diagenetic minerals. Society for Sedimentary Geology, US.

Goodfellow W, Lydon J, Turner R (1993) Geology and genesis of stratiform sediment-hosted (SEDEX) zinc-lead-silver sulphide deposits. Geological Association of Canada Special Paper 40:201-251.

Gu LX, Hu WX, He JX, Ni P, Xu KQ (2000) Regional variations in ore composition and fluid features of massive sulphide deposits in South China: Implications for genetic modelling. Episodes 23:110-118.

Gu LX, Zaw K, Hu WX, Zhang KJ, Ni P, He JX, Xu YT, Lu JJ, Lin CM (2007) Distinctive features of Late Palaeozoic massive sulphide deposits in South China. Ore Geology Reviews 31:107-138. doi: 10.1016/j.oregeorev.2005.01.002.

Guo JL, Gao S, Wu YB, Li M, Chen K, Hu ZC, Liang ZW, Liu YS, Zhou L, Zong KQ, Zhang W, Chen HH (2014) 3.45 Ga granitic gneisses from the Yangtze Craton, South China: Implications for Early Archean crustal growth. Precambrian Research 242:82-95. doi: 10.1016/j.precamres.2013.12.018.

Guo WM, Lu JJ, Jiang SY, Zhang RQ, Qi L (2011) Re-Os isotope dating of pyrite from the footwall mineralization zone of the Xinqiao deposit, Tongling, Anhui Province: Geochronological evidence for submarine exhalative sedimentation. Chinese Science Bulletin 56:3860-3865. doi: 10.1007/s11434-011-4770-y.

Hnatyshin D, Creaser RA, Wilkinson JJ, Gleeson SA (2015) Re-Os dating of pyrite confirms an early diagenetic onset and extended duration of mineralization in the Irish Zn-Pb ore field. Geology 43:143-146. doi: 10.1130/G36296.1.

Jiang SY, Palmer MR, Slack JF, Shaw DR (1998) Paragenesis and chemistry of multistage tourmaline formation in the Sullivan Pb-Zn-Ag deposit, British Columbia. Economic Geology and the Bulletin of the Society of Economic Geologists 93:47-67. doi: 10.2113/gsecongeo.93.1.47.

Lambert I, Scott K (1973) Implications of geochemical investigations of sedimentary rocks within and around the McArthur zinc-lead-silver deposit, Northern Territory. Journal of Geochemical Exploration 2:307-330.

Large D (1983) Sediment-hosted massive sulphide lead-zinc deposits: an empirical model In: Sangster DF (ed) Short Course Handbook. Mineral. Assoc. Canada, Canada, pp 1-30.

Leach D, Sangster D, Kelley K, Large R, Garven G, Allen C, Gutzmer J, Walters S (2005) Sediment-hosted lead-zinc deposits: A global perspective. Economic Geology 100:561-607.

Leach DL, Marsh E, Emsbo P, Rombach CS, Kelley KD, Anthonty M (2004) Nature of hydrothermal fluids at the shale-hosted Red Dog Zn-Pb-Ag deposits, Brooks Range, Alaska. Economic Geology 99:1449-1480. doi: 10.2113/99.7.1449.

Li DW, Fu ZR (1991) Multiple thrusting systems in the Middle and Lower Yangtze Metallognic Belt and their sinificance in mineralization. Earth Science-Journal of China University of Geosciences:670, 680. (In Chinese).

Li J-W, Li X-H, Pei R-F, Mei Y-X, Wang Y-L, Qu W-J, Huang X-B, Zang W-S (2007) Re-Os Age of Molybdenite from the Southern Ore Zone of the Wushan Copper Deposit, Jiangxi Province, and Its Geological Significance. Acta Geologica Sinica 81:801-807.

Li X-H, Liu Y, Li Q-L, Guo C-H, Chamberlain KR (2009) Precise determination of Phanerozoic zircon Pb/Pb age by multicollector SIMS without external standardization. Geochemistry, Geophysics, Geosystems 10:1-21. doi: 10.1029/2009gc002400.

Li XH, Li WX, Li ZX, Liu Y (2008) 850-790 Ma bimodal volcanic and intrusive rocks in northern Zhejiang, South China: A major episode of continental rift magmatism during the breakup of Rodinia. Lithos 102:341-357. doi: 10.1016/j.lithos.2007.04.007.

Li XH, Li WX, Li QL, Wang XC, Liu Y, Yang YH (2010a) Petrogenesis and tectonic significance of the similar to 850 Ma Gangbian alkaline complex in South China: Evidence from in situ zircon U-Pb dating, Hf-O isotopes and whole-rock geochemistry. Lithos 114:1-15. doi: 10.1016/j.lithos.2009.07.011.

Li XH, Li WX, Wang XC, Li QL, Liu Y, Tang GQ, Gao YY, Wu FY (2010b) SIMS U-Pb zircon geochronology of porphyry Cu-Au-(Mo) deposits in the Yangtze River Metallogenic Belt, eastern China: Magmatic response to early Cretaceous lithospheric extension. Lithos 119:427-438. doi: 10.1016/j.lithos.2010.07.018.

Li XH, Tang GQ, Gong B, Yang YH, Hou KJ, Hu ZC, Li QL, Liu Y, Li WX (2013) Qinghu zircon: A working reference for microbeam analysis of U-Pb age and Hf and O isotopes. Chinese Science Bulletin 58:4647-4654. doi: 10.1007/s11434-013-5932-x.

Li XH, Liu XM, Liu YS, Su L, Sun WD, Huang HQ, Yi K (2015) Accuracy of LA-ICPMS zircon U-Pb age determination: An inter-laboratory comparison. Sci China Earth Sci 58:1722-1730. doi: 10.1007/s11430-015-5110-x.

Li XJ (2006) Study of Ore Formation Conditions and Ore Deposit Models in Tongling Area, Anhui Province, China. China University of Geosciences, Beijing, pp 129. (In Chinese with English Abstract).

Li ZX, Li XH (2007) Formation of the 1300-km-wide intracontinental orogen and postorogenic magmatic province in Mesozoic South China: A flat-slab subduction model. Geology 35:179-182. doi: 10.1130/G23193a.1.

Liu YQ, Liu ZL, Yang CX (1984) Stable isotope studies of the Dongguashan Copper deposit in Tongling Prefecture, Anhui Province. Bulletin of the Institute of Mineral Deposits, Chinese Academy of Geological Sciences:70-101.

Liu YQ, Liu ZL (1991) Isotopes geochemistry and genesis of the stratiform massive copper (iron-sulfur) deposits in Tongling area, Anhui province. Bulletin of the Institute of Mineral Deposits, Chinese Academy of Geological Sciences 24:47-114. (In Chinese).

Lu S-M (2007) The Magmatism and Fluid Mineralizationin Shizishan Copper-gold Ore-field of Tongling, Anhui Province. Hefei University of Technology, pp 1-179.

Ludwig KR (2003) User's manual for Isoplot 3.00: a geochronological toolkit for Microsoft Excel. Kenneth R. Ludwig.

Mao J-W, Wang Y-T, Lehmann B, Yu J-J, Du A-D, Mei Y-X, Li Y-F, Zang W-S, Stein HJ, Zhou T-F (2006) Molybdenite Re–Os and albite ^{40}Ar ^{39}Ar dating of Cu–Au–Mo and magnetite porphyry systems in the Yangtze River valley and metallogenic implications. Ore Geology Reviews 29:307-324.

Mao JW, Xie GQ, Duan C, Pirajno F, Ishiyama D, Chen YC (2011) A tectono-genetic model for porphyry-skarn-stratabound Cu-Au-Mo-Fe and magnetite-apatite deposits along the Middle-Lower Yangtze River Valley, Eastern China. Ore Geology Reviews 43:294-314. doi: 10.1016/j.oregeorev.2011.07.010.

Matsuhisa Y (1974) ^{18}O/^{16}O ratios for NBS-28 and some silicate reference samples. Geochemical Journal 8:103-107.

Meinert LD (1982) Skarn, Manto, and Breccia Pipe Formation in Sedimentary-Rocks of the Cananea Mining District, Sonora, Mexico. Economic Geology 77:919-949.

Meinert LD, Hefton KK, Mayes D, Tasiran I (1997) Geology, zonation, and fluid evolution of the big Gossan Cu-Au skarn deposit, Ertsberg district: Irian Jaya. Economic Geology and the Bulletin of the Society of Economic Geologists 92:509-534. doi: 10.2113/gsecongeo.92.5.509.

Meinert LD, Hedenquist JW, Satoh H, Matsuhisa Y (2003) Formation of anhydrous and hydrous skarn in Cu-Au ore deposits by magmatic fluids. Economic Geology and the Bulletin of the Society of Economic Geologists 98:147-156. doi: Doi 10.2113/98.1.147.

Meinert LD, Dipple G, Nicolescu S (2005) World skarn deposits. Economic Geology 100:299-336.

Meng YF, Yang ZS, Zeng PS, Xu WY, Wang XC (2004) Tentative temporal constraints of ore-forming fluid systems in Tongling metallogenic province. Mineral Deposits 23:271-280. (In Chinese with English Abstract).

Mezger K, Krogstad EJ (1997) Interpretation of discordant U-Pb zircon ages: An evaluation. Journal of Metamorphic Geology 15:127-140. doi: DOI 10.1111/j.1525-1314.1997.00008.x.

Nakai S, Halliday AN, Kesler SE, Jones HD, Kyle JR, Lane TE (1993) Rb-Sr Dating of Sphalerites from Mississippi Valley-Type (Mvt) Ore-Deposits. Geochimica Et Cosmochimica Acta 57:417-427. doi: Doi 10.1016/0016-7037(93)90440-8.

Nesbitt BE, Longstaffe FJ, Shaw DR, Muehlenbachs K (1984) Oxygen Isotope Geochemistry of the Sullivan Massive Sulfide Deposit, Kimberley, British-Columbia. Economic Geology 79:933-946. doi: 10.2113/gsecongeo.79.5.933.

Ostendorf J, Henjes-Kunst F, Mondillo N, Boni M, Schneider J, Gutzmer J (2015) Formation of Mississippi Valley-type deposits linked to hydrocarbon generation in extensional tectonic settings: Evidence from the Jabali Zn-Pb-(Ag) deposit (Yemen). Geology 43:1055-1058. doi: 10.1130/G37112.1.

Pan YM, Dong P (1999) The Lower Changjiang (Yangzi/Yangtze River) metallogenic belt, east central China: intrusion- and wall rock-hosted Cu-Fe-Au, Mo, Zn, Pb, Ag deposits. Ore Geology Reviews 15:177-242. doi: Doi 10.1016/S0169-1368(99)00022-0.

Roedder E (1984) Fluid Inclusions. Mineralogical Society of America, US.

Sato T (1984) Manto type copper deposits in Chile: a review. Bulletin of the geological survey of Japan 35:565-582.

Schoene B (2014) 4.10 - U–Th–Pb Geochronology In: Turekian HDHK (ed) Treatise on Geochemistry (Second Edition). Elsevier, Oxford, pp 341-378.

Selby D, Creaser RA (2001) Re-Os geochronology and systematics in molybdenite from the Endako porphyry molybdenum deposit, British Columbia, Canada. Economic Geology and the Bulletin of the Society of Economic Geologists 96:197-204. doi: Doi 10.2113/96.1.197.

Selby D, Kelley KD, Hitzman MW, Zieg J (2009) Re-Os sulfide (bornite, chalcopyrite, and pyrite) systematics of the carbonate-hosted copper deposits at Ruby Creek, Southern Brooks Range, Alaska. Economic Geology 104:437-444.

Slack JF, Selby D, Dumoulin JA (2015) Hydrothermal, Biogenic, and Seawater Components in Metalliferous Black Shales of the Brooks Range, Alaska: Synsedimentary Metal Enrichment in a Carbonate Ramp Setting. Economic Geology 110:653-675.

Sláma J, Košler J, Condon DJ, Crowley JL, Gerdes A, Hanchar JM, Horstwood MS, Morris GA, Nasdala L, Norberg N (2008) Plešovice zircon—a new natural reference material for U–Pb and Hf isotopic microanalysis. Chemical Geology 249:1-35.

Stacey Jt, Kramers J (1975) Approximation of terrestrial lead isotope evolution by a two-stage model. Earth and Planetary Science Letters 26:207-221.

Stein HJ, Morgan JW, Schersten A (2000) Re-Os Dating of Low-Level Highly Radiogenic (LLHR) Sulfides:The Harnas Gold Deposit, Southwest Sweden, Records Continental-Scale TectonicEvents. Economic Geology 95:1657-1671. doi: 10.2113/gsecongeo.95.8.1657.

Wan TF (2012) The Tectonics of China: Data, Maps and Evolution. Springer, Beijing, China.

Wang GG, Ni P (2009) Fluid inclusions study for the pyrite vein beneath Xinqiao stritiform massive Cu deposit. Acta Mineralogica Sinica. pp 256 (In Chinese).

Wang YB, Liu DY, Meng YF, Zeng PS, Yang ZS, Tian SH (2004) SHRIMP U-Pb geochronology of the Xinqiao Cu-S-Fe-Au deposit in the Tongling ore district, Anhui. Geology in China 31:169-173.

Wang YB, Tang SH, Wang JH, Zeng PS, Yang ZS, Meng YF, Tian SH (2005) Rb-Sr Dating the Pyrite of the Xinqiao Cu-S-Fe-Au Deposit, Tongling, Anhui Province. Geological Review 50:538-542. (In Chinese with English Abstract).

Wendt I, Carl C (1991) The Statistical Distribution of the Mean Squared Weighted Deviation. Chemical Geology 86:275-285. doi: Doi 10.1016/0168-9622(91)90010-T.

Wu C-L (1996) ^{40}Ar- ^{39}Ar Chronology of Intrusive Rocks from Tongling. Acta Petrologica Et Mineralogica 15:299-306.

Wu GG, Zhang D, Zang WS (2003) Study of tectonic layering motion and layering mineralization in the Tongling metallogenic cluster. Science in China Series D-Earth Sciences 46:852-863. doi: 10.1360/03yd0204.

Wu GG, Zhang D, Di YJ, Zang WS, Zhang XX, Song B, Zhang ZY (2009) SHRIMP Zircon U-Pb daing for Intrusions in Tongling mining districts and implications for geodynamics. Science China Earth Sciences 38:630-645. (In Chinese with English Abstract). doi: http://earth.scichina.com:8080/sciD/CN/

Wu L-S, Zou X-Q (1997) Re-Os isotopic age study of the Chengmenshan copper deposit, Jiangxi Province. Mineral Deposits 16:376-381.

Xiao X, Zhou TF, Fan Y, Xie J, ZHang LJ (2016) LA-ICP-MS in situ trace elements and FE-SEM analysis of pyrite from the Xinqiao Cu-Au-S deposit in Tongling, Anhui and its constraints on the ore genesis. Acta Petrologica Sinica 32:369-376.

Xiao XJ, Gu LX, Ni P (2002) Multi-episode fluid boiling in the Shizishan copper-gold deposit at Tongling, Anhui Province: its bearing on ore formation. Science in China Series D-Earth Sciences 45:34-44. doi: Doi 10.1007/Bf02879694.

Xie JC, Yang XY, Sun WD, Du JG, Xu W, Wu LB, Wang KY, Du XW (2009) Geochronological and geochemical constraints on formation of the Tongling metal deposits, middle Yangtze metallogenic belt, east-central China. International Geology Review 51:388-421. doi: doi:10.1080/00206810802712004.

Xie QQ, Chen TH, Fan ZL, Xu XC, Zhou YF, Shi WB, Xue JJ (2014) Morphological characteristics and genesis of colloform pyrite in Xinqiao Fe-S deposit, Tongling, Anhui Province (in Chinese). Science in China Series D: Earth Sciences 44:2665-2674. (In Chinese with English Abstract).

Xu G, Zhou J (2001) The Xinqiao Cu-S-Fe-Au deposit in the Tongling mineral district, China: synorogenic remobilization of a stratiform sulfide deposit. Ore Geology Reviews 18:77-94. doi: Doi 10.1016/S0169-1368(01)00017-8.

Xu WY, Yang ZS, Meng YF, Zeng PS, Shi DN, Tian SH, Li HY (2004) Genetic model and dynamic migration of ore-forming fluids in carboniferous exhalation-sedimentary massive sulfide deposits of Tongling district, Anhui Province. Mineral Deposits 23:353-363. (In Chinese with English Abstract).

Xu XC, Yin T, Lou JW, Lu SM, Xie QQ, Chu PL (2010) Origin of Dongguashan stratabound Cu-Au skarn deposit in Tongling: Restraints of sulfur isotope. Acta Petrologica Sinica 26:2739-2750. (In Chinese with English Abstract).

Yang SY, Jiang SY, Li L, Sun Y, Sun MZ, Bian LZ, Xiong YG, Cao ZQ (2011a) Late Mesozoic magmatism of the Jiurui mineralization district in the Middle-Lower Yangtze River Metallogenic Belt, Eastern China: Precise U-Pb ages and geodynamic implications. Gondwana Research 20:831-843. doi: 10.1016/j.gr.2011.03.012.

Yang XN, Xu ZW, Lu XC, Jiang SY, Ling HF, Liu LG, Chen DY (2011b) Porphyry and skarn Au-Cu deposits in the Shizishan orefield, Tongling, East China: U-Pb dating and in-situ Hf isotope analysis of zircons and petrogenesis of associated granitoids. Ore Geology Reviews 43:182-193. doi: 10.1016/j.oregeorev.2010.09.003.

Yuan F, Song YL, Wang SW, Zhou TF, Sun WA (2014) Characteristics of porphyry mineralization in the depth of Dongguashan deposit and its relationship with skarn-type mineralization. Chinese Journal of Geology 49:588-607. (In Chinese with English Abstract).

Zhang Y, Shao YJ, Quan W, Liu ZF, Liu QQ (2015) Rb-Sr Isotope Dating of the Fluid Inclusions in Quartz from Quartz-Pyrite Veins in the Footwall of Xinqiao Cu-S-Fe Deposit, Tongling. Geological Review 61:1168-1176.

Zhao JH, Zhou MF, Yan DP, Zheng JP, Li JW (2011) Reappraisal of the ages of Neoproterozoic strata in South China: No connection with the Grenvillian orogeny. Geology 39:299-302. doi: 10.1130/G31701.1.

Zhao R, Xie YH, Yao YY, He WG (1985) S isotopes study for Chengmenshan and Wushan Cu deposits. Chinese Journal of Geology 3:251-258. (In Chinese).

Zhou TF, Yu F, Yuan F (2008) Advances on petrogensis and metallogeny study of the mineralization belt of the Middle and Lower Reaches of the Yangtze River area. Acta Petrologica Sinica 24:1665-1678.

Zhou TF, ZHang LJ, Yuan F, Fan Y (2010) LA-ICP-MS in situ trace element analysis of pyrite from the Xinqiao C-Au-S Deposit in Tongling, Anhui, and its constraints on the ore genesis. Earth Science Frontiers 17:306-319.

Zhou WK, Chen SY, Zhao SL, Cheng QF, Mao JR, Qiu YQ (1983) The Volcanics in north ore zone of the copper deposit in Wushan, Jiangxi Province. Bulletin of Nanjing Institute of Geology and Mineral Resources 4:47-62. (In Chinese).

Zhou Z (1984) Genesis for Mashan Au deposit, Tongling. Geological Review 30:467-476. (In Chinese).

List of Tables and Figures

Table 1. SIMS zircon U-Pb data of the Xinqiao stock quartz diorite and an unaltered diorite porphyry.

Table 2. SIMS quartz oxygen isotope data of banded quartz veins from the skarn ore and pyrite-quartz veins hosted by the Gaolishan Formation sandstone.

Table3. Re-Os data of pyrite samples from the stratabound massive orebody at Xinqiao.

Table4. Published geochronology data for the strataform massive sulfide deposits and Cretaceous intrusions and associated porphyry-skarn deposits along Middle and Lower Metallogenic Belt.

Fig.1. Geological map showing the igneous rocks distribution in the mining districts along the Middle and Lower Metallogenic Belt, with the insert illustrating the geological setting of China. Revised after Mao et al. (2011).

Fig.2. Stratigraphic column of sedimentary rocks exposed in the Xinqiao mining area. Revised after 803-Geological-Team (1971).

Fig.3.A). Geological map of Xinqiao deposit; B-C). Representative cross sections of Xinqiao deposit, with samples location marked in B. Revised after 803-Geological-Team (1971). See text for detailed information.

Fig.4.Massive pyrite ore occurs as veins in Permian Qixia Formation limestone. Revised after 803-Geological-Team (1971).

Fig. 5. A). Cu, S, Au and Ag grade distribution in the main stratabound orebody at Xinqiao, which shows strong relationship to the distance from the Jitou stock. The location of the Jitou stock is between the exploration lines 15 and 26; B). Distribution of massive pyrite ore, massive chalcopyrite ore, massive pyrite ore, massive magnetite ore and Pb-Zn mineralization at Xinqiao, which show a close association with the Jitou stock exhibiting concentric zoning, see text for discussion. Revised after 803-Geological-Team (1971).

Fig. 6. Igneous rocks, alteration and mineralization assemblages of the Xinqiao deposit. A). Fresh quartz diorite from the central phase of the Jitou stock; B). Diorite porphyry from the

marginal phase of the Jitou stock, with quartz vein and feldspar dissolution vugs indicating intensive alteration; C). Alteration-free diorite porphyry observed in the open pit; D). Red-brown garnet skarn with hematite and calcite; E). Banded wollastonite skarn in silicified limestone with garnet and diopside, the wollastonite clusters exhibit radiating textures; F).Radiating clusters of epidote in the alterated diorite porphyry; G). Clusters of chlorite in diorite porphyry; H). Pyrite-calcite vein in massive magnetite ore; I). Banded quartz and pyrite veins from the skarn ore; J). Massive pyrite ore comprising massive anhedral grains with a pale colour; K). A cluster of cubic pyrite ore; L). Massive colloform pyrite ore with cluster and vein comprised of crystallized pyrite; M). Massive chalcopyrite ore; N). Sphalerite-pyrite-calcite vein in limestone; O). Pyrite-quartz vein in Gaolishan Formation sandstone, the pyrite are coarse grained. See text for detailed description.

Fig. 7. Photomicrographs and scanning electron microscope (SEM) images illustrating the petrographic characteristics of the sulfides and quartz at Xinqiao. A) Euhedral pyrites grains; B) Anhedral pyrite grains; C) Colloform pyrite grains; D) Massive chalcopyrite ore with pyrite and magnetite; E) Pyrite, quartz and carbonate minerals from garnet bearing skarn ore; F) Anhedral quartz with pyrite grains from pyrite-quartz veins hosted by the Gaolishan Formation sandstone. Pyrite sample from A and B are used for Re-Os dating, quartz grains from E and F are used for SIMS oxygen analysis. See text for details.

Fig.8. Alteration and mineralization paragenesis at Xinqiao. Revised after (803-Geological-Team 1971).

Fig.9. Fluid inclusions hosted by diopside and quartz grains. A-B) Diopside hosted pseudosecondary liquid-vapor fluid inclusions with and without halite minerals from the skarn ore; C) Liquid-vapour two-phase fluid inclusions hosted by quartz grains form the banded pyrite-quartz skarn ore; D) Liquid-vapor two-phase fluid inclusions hosted by quartz grains from the pyrite-quartz veins in the Gaolishan Formation sandstone.

Fig.10. Homogenization temperature-salinity plot of the fluid inclusions associated with the skarn ore and the pyrite-quartz veins in the Gaolishan Formation sandstone. Also presented are the quartz hosted fluid inclusions data from the Red Dog Pb-Zn deposit (Leach et al. 2004). See text for detailed information.

Fig.11. SIMS quartz oxygen isotope data of the quartz bearing skarn ore and pyrite-quartz veins in the Gaolishan Formation sandstone, and the calculated fluid oxygen isotopic compositions based on fluid inclusion homogenization temperatures in this study. See text for detailed discussion.

Fig.12. Wetherill concordia plots and weighted average $^{206}Pb/^{238}U$ ages of the zircons from the igneous rocks at Xinqiao. A and C are data for the marginal phase quartz diorite from the Jitou stock; B and D are data for the alteration free diorite porphyry distributed in the open pit, see text for details.

Fig.13. Isochron plot showing the pyrite Re-Os data analysed in this study. Also presented are the 320 Ma and 138 Ma reference lines. See text for discussion.

Fig.14. A) Published pyrite sulfur isotopic data of the Carboniferous sedimentary rocks, Cretaceous igneous rocks and associated porphyry-skarn deposits within Middle and Lower Yangtze Metallogenic Belt; B) Published pyrite sulfur isotopic data of the stratabound deposits in Middle and Lower Yangtze Metallogenic Belt, also showing is data from Red Dog deposit. Data are from (Zhou et al. 1983; Liu et al. 1984; Zhou 1984; Zhao et al. 1985; Pan and Dong 1999; Leach et al. 2004; Xu et al. 2004; Li 2006; Xu et al. 2010). See text for discussion.

Fig.15. Published geochronology data of the Cretaceous igneous rocks, associated porphyry-skarn deposits and stratabound massive sulfide deposits in Middle and Lower Yangtze Metallogenic Belt. Data are from (Wu 1996; Wu and Zou 1997; Meng et al. 2004; Wang et al. 2004; Xu et al. 2004; Ding et al. 2005; Wang et al. 2005; Mao et al. 2006; Li et al. 2007; Lu 2007; Wu et al. 2009; Xie et al. 2009; Li et al. 2010b; Guo et al. 2011; Yang et al. 2011a; Yang et al. 2011b). See text for discussion.

Fig.16. Soil Cu, Pb, Zn, Au and Ag geochemical anomaly map for the Tongling mining district (Jiujiang conference communication, 2010, unpublished data).

Table 1. SIMS quartz oxygen isotope data of the skarn ore and pyrite quartz veins in Gaolishan Forma

Sample No.	$\delta^{18}O$ ‰	2σ
quartz from the sakrn ore		
XQ5-1_1	12.85	0.34
XQ5-1_2	11.09	0.18
XQ5-1_3	12.22	0.33
XQ5-1_4	12.80	0.25
XQ5-1_5	13.25	0.34
XQ5-1_6	12.47	0.27
XQ5-1_7	13.69	0.37
XQ5-1_8	12.54	0.37
XQ5-1_9	13.79	0.22
XQ5-1_10	12.02	0.41
XQ5-1_11	12.16	0.25
XQ5-2_1	11.99	0.42
XQ5-2_2	12.25	0.31
XQ5-2_3	11.65	0.38
XQ5-2_4	12.72	0.27
XQ5-2_5	12.23	0.28
XQ5-2_6	12.02	0.35
XQ5-2_7	15.68	0.28
XQ5-2_8	12.17	0.28
XQ5-2_9	14.31	0.40
XQ5-2_10	12.52	0.35
XQ5-3_1	12.22	0.31
XQ5-3_2	16.03	0.30
XQ5-3_3	11.44	0.44
XQ5-3_4	11.79	0.33
XQ5-3_5	13.23	0.35
XQ5-3_6	12.42	0.36
XQ5-3_7	12.50	0.36
XQ5-3_8	11.98	0.35
XQ5-3_9	12.54	0.30
XQ5-3_10	12.28	0.38
XQ5-3_11	12.27	0.26
quartz from vein nettworks in the Gaolishan Formation sandstone		
XQ8-1_1	14.16	0.30
XQ8-1_2	15.21	0.30
XQ8-1_3	14.36	0.49
XQ8-1_4	15.60	0.31
XQ8-1_5	14.40	0.24
XQ8-1_6	15.52	0.31
XQ8-1_7	14.80	0.41
XQ8-1_8	14.92	0.32
XQ8-1_9	14.10	0.29
XQ8-1_10	14.57	0.54
XQ8-1_11	15.44	0.36

XQ8-1_12	15.45	0.31
XQ8-1_13	14.37	0.29
XQ8-2_1	20.28	0.35
XQ8-2_2	17.10	0.21
XQ8-2_3	14.69	0.36
XQ8-2_4	16.07	0.18
XQ8-2_5	16.74	0.33
XQ8-2_6	14.44	0.26
XQ8-2_7	15.24	0.34
XQ8-2_8	17.21	0.28
XQ8-2_9	19.93	0.35
XQ8-2_10	13.47	0.50
XQ8-2_11	15.08	0.41
XQ8-2_12	19.06	0.35
XQ8-2_13	15.90	0.31
XQ8-3_1	15.03	0.26
XQ8-3_2	16.86	0.37
XQ8-3_3	16.57	0.31
XQ8-3_4	14.89	0.45
XQ8-3_5	15.99	0.38
XQ8-3_6	15.55	0.28
XQ8-3_7	15.85	0.32
XQ8-3_8	16.00	0.44
XQ8-3_9	15.89	0.43
XQ8-3_10	15.68	0.28
XQ8-4_1	16.55	0.27
XQ8-4_2	16.35	0.38
XQ8-4_3	19.30	0.38
XQ8-4_4	14.77	0.26
XQ8-4_5	15.33	0.86
XQ8-4_6	10.16	0.40
XQ8-4_7	10.51	0.30
XQ8-4_8	16.94	0.24
XQ8-4_9	17.13	0.28
XQ8-5_1	14.51	0.22
XQ8-5_2	12.53	0.38
XQ8-5_3	17.07	0.38
XQ8-5_4	16.27	0.33
XQ8-5_5	16.82	0.24
XQ8-5_6	13.73	0.30
XQ8-5_7	16.31	0.22
XQ8-5_8	17.09	0.33
XQ8-5_9	13.72	0.28
XQ8-5_10	17.76	0.32
XQ8-5_11	15.62	0.47
XQ8-5_12	16.43	0.21
XQ8-5_13	12.22	0.33
XQ8-5_14	15.27	0.45

XQ8-6_1	16.43	0.27
XQ8-6_2	15.43	0.37
XQ8-6_3	16.26	0.35
XQ8-6_4	15.54	0.42
XQ8-6_5	15.26	0.46
XQ8-6_6	17.67	0.39
XQ8-6_7	13.87	0.36
XQ8-6_8	15.89	0.34
XQ8-6_9	16.15	0.31
XQ8-6_10	15.39	0.40
XQ8-6_11	16.48	0.39
XQ8-6_12	13.70	0.48

Table 2. SIMS zircon U-Pb data of the quartz diorite and diorite porphyry samples at Xinqiao.

Sample No.	U ppm	Th ppm	Th/U	$f^{206}Pb$ %	$^{207}Pb/^{206}Pb$	±1σ %	$^{207}Pb/^{235}U$	±1σ %
Central phase quartz diorite of the Jitou pluton								
XQ09-3@01	232	242	1.04	0.3	0.04939	3.22	0.14156	3.95
XQ09-3@02	99	54	0.54	1.1	0.04734	4.04	0.13985	4.34
XQ09-3@03	209	152	0.73	0.2	0.05104	2.68	0.14676	3.74
XQ09-3@04	109	99	0.91	0.8	0.04984	3.77	0.14904	4.17
XQ09-3@07	167	114	0.68	0.4	0.04943	3.04	0.13937	4.78
XQ09-3@08	261	206	0.79	0.3	0.05228	2.39	0.14985	3.88
XQ09-3@10	214	206	0.97	0.1	0.05260	2.64	0.15443	3.29
XQ09-3@12	175	68	0.39	0.2	0.04899	3.02	0.14864	3.40
XQ09-3@13	114	77	0.67	0.9	0.05100	4.15	0.15218	4.44
XQ09-3@14	186	143	0.77	0.3	0.04988	2.89	0.14933	3.28
XQ09-3@15	204	167	0.82	0.3	0.04893	3.08	0.14906	3.44
XQ09-3@16	151	111	0.73	0.6	0.05235	3.13	0.14291	5.40
XQ09-3@17	132	105	0.79	0.4	0.04929	4.22	0.14847	4.50
XQ09-3@18	300	301	1.00	0.5	0.05160	2.27	0.14176	4.16
XQ09-3@19	171	128	0.75	0.0	0.05025	3.04	0.14918	3.40
XQ09-3@20	203	216	1.07	0.3	0.04851	2.84	0.14487	3.24
Post-ore diorite porphyry								
XQ-1@01	466	213	0.46	0.2	0.04745	1.35	0.13398	2.03
XQ-1@02	794	365	0.46	0.1	0.04820	1.29	0.13562	2.05
XQ-1@03	807	452	0.56	0.1	0.04838	1.08	0.13763	1.85
XQ-1@04	810	359	0.44	0.1	0.04746	0.94	0.13325	1.81
XQ-1@05	810	504	0.62	0.0	0.04897	1.00	0.14153	1.80
XQ-1@06	294	149	0.51	0.1	0.04919	1.50	0.13965	2.15
XQ-1@07	993	541	0.55	0.1	0.04935	0.69	0.14218	1.66
XQ-1@09	510	196	0.38	0.2	0.04768	1.59	0.13462	2.19
XQ-1@10	467	217	0.47	0.2	0.04806	1.75	0.13267	2.32
XQ-1@11	811	411	0.51	0.1	0.04928	1.04	0.13754	1.82
XQ-1@12	472	335	0.71	0.3	0.04687	1.58	0.12993	2.19
XQ-1@14	764	453	0.59	0.2	0.04779	1.12	0.13309	1.93
XQ-1@15	417	269	0.65	0.1	0.04848	1.23	0.14168	1.94
XQ-1@16	474	190	0.40	0.1	0.04928	1.08	0.14057	1.87
XQ-1@17	609	291	0.48	0.1	0.04949	0.91	0.13951	1.77
XQ-1@18	571	252	0.44	0.1	0.04903	0.91	0.14170	1.80
XQ-1@19	448	264	0.59	0.2	0.04770	1.41	0.13468	2.13
XQ-1@20	446	247	0.55	0.2	0.04686	1.53	0.13286	2.14
XQ-1@22	837	482	0.58	0.1	0.04858	0.82	0.13501	1.77
XQ-1@23	405	261	0.64	0.1	0.04982	1.39	0.13937	2.06
XQ-1@25	902	496	0.55	0.2	0.04811	1.70	0.13697	2.28
XQ-1@26	468	204	0.43	0.1	0.05021	1.51	0.13795	2.14

$^{206}Pb/^{238}U$	±1σ %	rho	$t^{207}Pb/^{235}U$ Ma	±1σ abs	$t^{206}Pb/^{238}U$ Ma	±1σ abs
0.02167	1.51	0.38	134.4	5.0	138.2	2.1
0.02142	1.59	0.37	132.9	5.4	136.6	2.1
0.02167	1.55	0.42	139.0	4.9	138.2	2.1
0.02169	1.77	0.43	141.1	5.5	138.3	2.4
0.02173	1.53	0.32	132.5	6.0	138.6	2.1
0.02178	1.50	0.39	141.8	5.1	138.9	2.1
0.02165	1.51	0.46	145.8	4.5	138.0	2.1
0.02200	1.55	0.46	140.7	4.5	140.3	2.2
0.02164	1.59	0.36	143.8	6.0	138.0	2.2
0.02171	1.56	0.47	141.3	4.3	138.5	2.1
0.02209	1.53	0.44	141.1	4.5	140.9	2.1
0.02181	1.58	0.29	135.6	6.9	139.1	2.2
0.02184	1.58	0.35	140.6	5.9	139.3	2.2
0.02155	1.51	0.36	134.6	5.3	137.5	2.1
0.02153	1.52	0.45	141.2	4.5	137.3	2.1
0.02166	1.55	0.48	137.4	4.2	138.2	2.1
0.02048	1.53	0.75	127.7	2.4	130.7	2.0
0.02041	1.60	0.78	129.1	2.5	130.2	2.1
0.02063	1.50	0.81	130.9	2.3	131.6	2.0
0.02036	1.55	0.86	127.0	2.2	129.9	2.0
0.02096	1.50	0.83	134.4	2.3	133.7	2.0
0.02059	1.54	0.72	132.7	2.7	131.4	2.0
0.02089	1.51	0.91	135.0	2.1	133.3	2.0
0.02048	1.51	0.69	128.2	2.6	130.7	2.0
0.02002	1.52	0.66	126.5	2.8	127.8	1.9
0.02024	1.50	0.82	130.8	2.2	129.2	1.9
0.02011	1.52	0.69	124.0	2.6	128.3	1.9
0.02020	1.57	0.81	126.9	2.3	128.9	2.0
0.02119	1.50	0.77	134.5	2.4	135.2	2.0
0.02069	1.53	0.82	133.5	2.3	132.0	2.0
0.02044	1.52	0.86	132.6	2.2	130.5	2.0
0.02096	1.55	0.86	134.6	2.3	133.7	2.1
0.02048	1.60	0.75	128.3	2.6	130.7	2.1
0.02056	1.50	0.70	126.7	2.6	131.2	2.0
0.02015	1.57	0.89	128.6	2.1	128.6	2.0
0.02029	1.52	0.74	132.5	2.6	129.5	1.9
0.02065	1.52	0.67	130.3	2.8	131.8	2.0
0.01993	1.51	0.71	131.2	2.6	127.2	1.9

Table 3. Pyrite Re-Os data of the stratabound massive orebody at Xinqiao.

Sample No.	Re ppb	±	Os ppt	±	^{192}Os ppt	±	^{187}Re/^{188}Os	±	^{187}Os/^{188}Os
XQ15*	1.10	0.01	31.8	0.4	11.0	0.3	198.1	5.8	1.60
XQ24	31.88	0.12	124.7	2.2	26.0	0.6	2439.5	57.3	7.64
XQ25	28.87	0.11	64.3	4.1	9.0	0.6	6377.7	420.8	15.07
XQ10	26.05	0.10	50.9	7.0	3.9	0.4	14870.1	1715.6	38.70

±	rho	initial $^{187}Os/^{188}Os$ @320 Ma	±	initial $^{187}Os/^{188}Os$ @138 Ma	±
0.05	0.925	0.5	0.1	1.1	0.1
0.18	0.985	-5.4	0.5	2.0	0.3
0.99	0.997	-18.9	3.2	0.4	1.9
4.46	0.999	-40.6	13.4	4.5	8.3

Table 4. Geochronology data for stratiform massive sulfide deposits and Meosozoic intrusions and deposits a

Deposit	Sample type	Age/Ma	Method
Wushan	Granodiorite-porphyry	148.0±1.0	LA-ICP-MS Zircon U-Pb
	Granodiorite-porphyry	147.3±0.9	LA-ICP-MS Zircon U-Pb
	Granodiorite-porphyry	145.4±0.9	LA-ICP-MS Zircon U-Pb
	Lamprophyre	144.3±0.9	LA-ICP-MS Zircon U-Pb
	Lamprophyre	143.6±0.9	LA-ICP-MS Zircon U-Pb
	Mafic dike	144.5±1.2	LA-ICP-MS Zircon U-Pb
	Mafic dike	142.6±1.0	LA-ICP-MS Zircon U-Pb
	Granodiorite-porphyry	146.6±1.0	SIMS Zircon U-Pb
	Granodiorite-porphyry	146.2±1.2	SIMS Zircon U-Pb
	Granodiorite-porphyry	144.6±3.9	SIMS Zircon U-Pb
	Skarn orebody	146.4±2.6	Molybdenite Re-Os
Chengmenshan	Granodiorite-porphyry	144.5±1.3	SIMS Zircon U-Pb
	Porphyry Cu	137.0±3	Molybdenite Re-Os
	Porphyry Cu	141.0±3	Molybdenite Re-Os
	Porphyry Cu	142.3±2.3	Molybdenite Re-Os
Dongguashan	Quartz monzodiorite	138.8±1.6	LA-ICP-MS Zircon U-Pb
	Quartz monzodiorite	135.6±1.4	Whole rock Rb-Sr
	Pyroxene monzonite	148.2±3.1	SHRIMP Zircon U-Pb
	Quartz monzodiorite	135.5±2.2	SHRIMP Zircon U-Pb
	Quartz monzodiorite	135.8±1.1	Biotite Ar-Ar
	Porphyry-Skarn Cu	137.4(?)	Pyrite Re-Os model age
Xinqiao	Monzodiorite	146.4±4.3	SHRIMP Zircon U-Pb
	Quartz monzodiorite	140.4±2.2	SHRIMP Zircon U-Pb
	Pyrite vein in sandstone	319±13	Pyrite Re-Os isochron
	Stratiform orebody	112.6±7.8	Pyrite Rb-Sr isochron
	Stratiform orebody	126±11	Pyrite Re-Os isochron
Simenkou	Stratiform orebody	303±33	Pyrite Re-Os isochron
Jinkouyu	Stratiform orebody	137±0.19	Pyrite Re-Os isochron

along MLYMB

References
(Ding et al., 2005; Yang et al., 2011a)
(Li et al., 2010c)
(Li et al., 2007)
(Li et al., 2010c)
(Wu and Zou, 1997)
(Mao et al., 2006)
(Yang et al., 2011b) (Xu et al., 2004b) (Wu et al., 2009) (Lu, 2007) (Wu, 1996) (Meng et al., 2004)
(Wu et al., 2009)
(Guo et al., 2011) (Wang et al., 2005) (Xie et al., 2009)
(Meng et al., 2004)

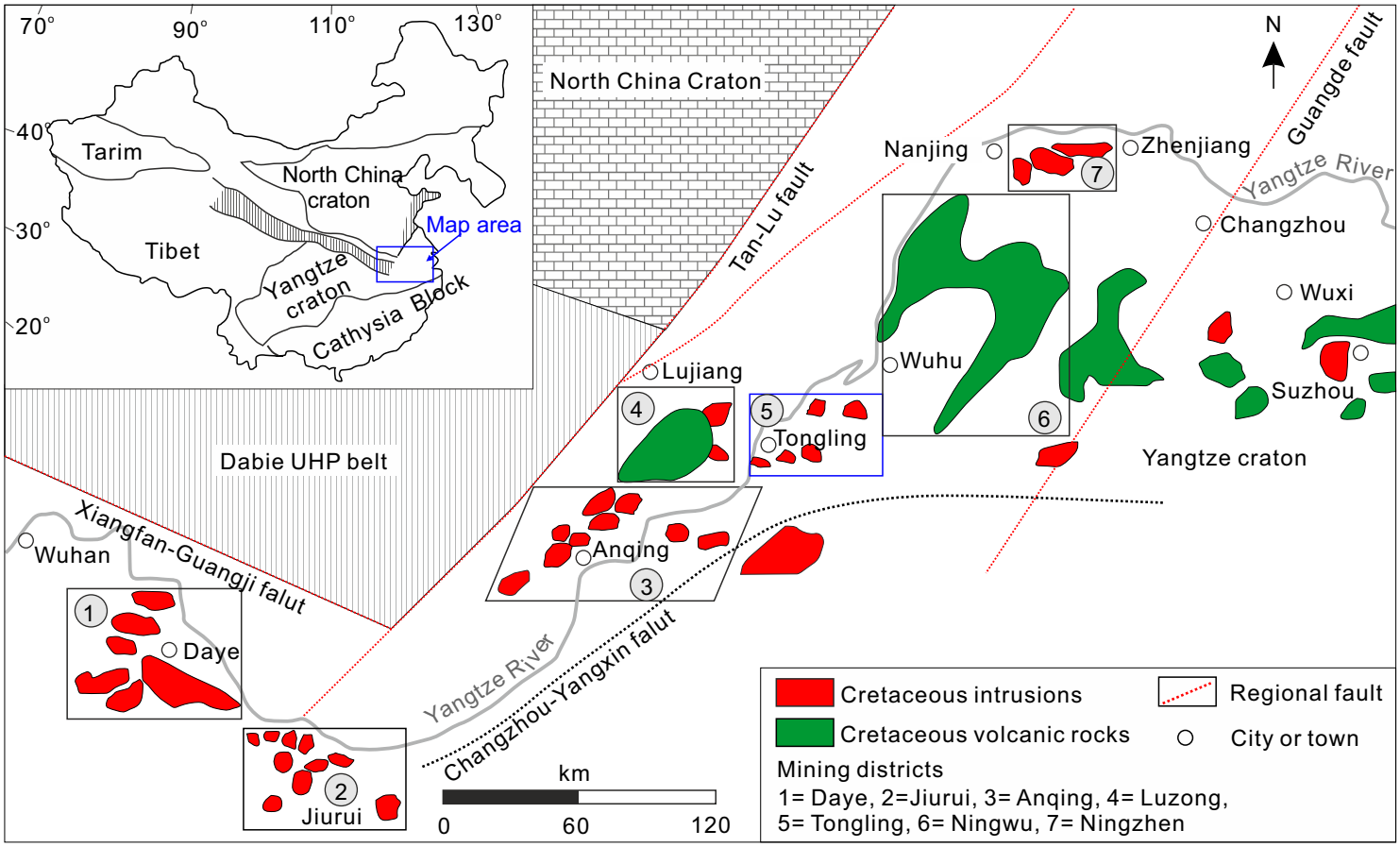
70°
90°
110°
130°
40°
30°
20°
Tarim
North China craton
Tibet
Yangtze craton
Cathysia Block
Map area
North China Craton
Tan-Lu fault
Guangde fault
N
Nanjing
Zhenjiang
Yangtze River
Changzhou
Wuxi
Suzhou
Wuhu
Lujiang
Tongling
Anqing
Yangtze craton
Dabie UHP belt
Xiangfan-Guangji falut
Wuhan
Daye
Jiurui
Yangtze River
Changzhou-Yangxin falut
km
0
60
120
Cretaceous intrusions
Cretaceous volcanic rocks
Regional fault
City or town
Mining districts
1= Daye, 2=Jiurui, 3= Anqing, 4= Luzong,
5= Tongling, 6= Ningwu, 7= Ningzhen

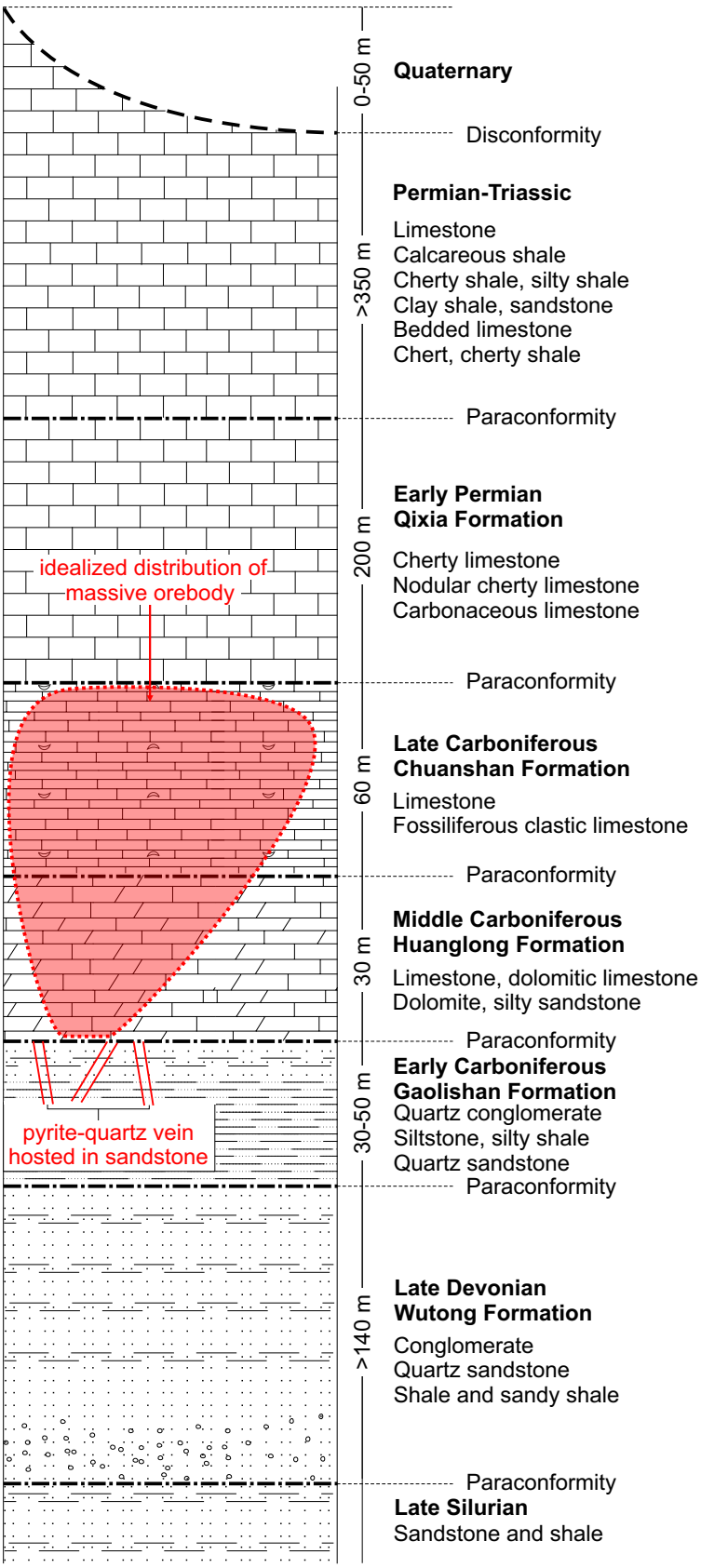
0-50 m
Quaternary
Disconformity
Permian-Triassic
Limestone
Calcareous shale
Cherty shale, silty shale
Clay shale, sandstone
Bedded limestone
Chert, cherty shale
>350 m
Paraconformity
Early Permian
Qixia Formation
Cherty limestone
Nodular cherty limestone
Carbonaceous limestone
200 m
idealized distribution of massive orebody
Paraconformity
Late Carboniferous
Chuanshan Formation
Limestone
Fossiliferous clastic limestone
60 m
Paraconformity
Middle Carboniferous
Huanglong Formation
Limestone, dolomitic limestone
Dolomite, silty sandstone
30 m
Paraconformity
Early Carboniferous
Gaolishan Formation
Quartz conglomerate
Siltstone, silty shale
Quartz sandstone
30-50 m
pyrite-quartz vein hosted in sandstone
Paraconformity
Late Devonian
Wutong Formation
Conglomerate
Quartz sandstone
Shale and sandy shale
>140 m
Paraconformity
Late Silurian
Sandstone and shale

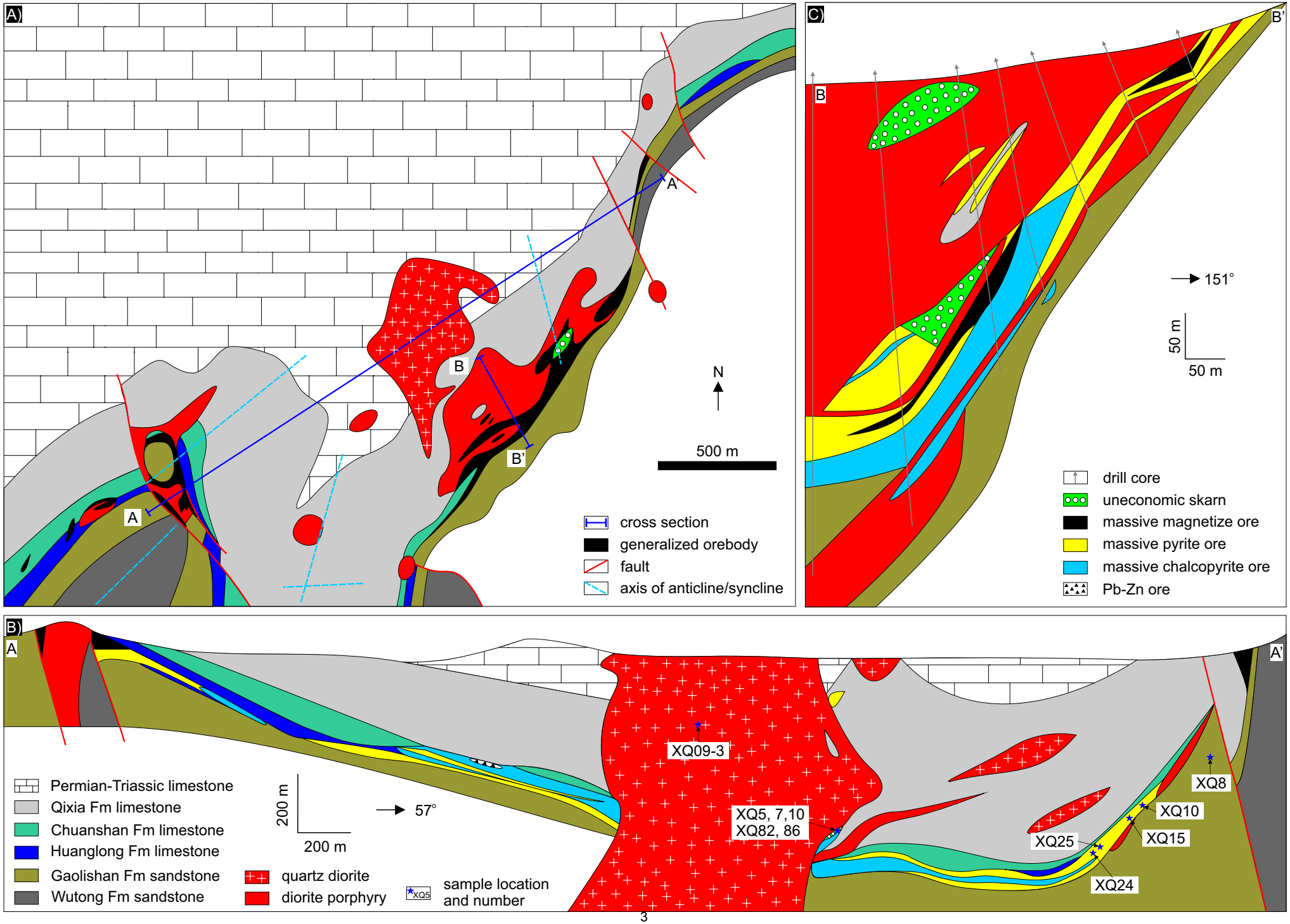
A)
A
A'
B
B'
N
500 m
cross section
generalized orebody
fault
axis of anticline/syncline
C)
B
B'
151°
50 m
50 m
drill core
uneconomic skarn
massive magnetize ore
massive pyrite ore
massive chalcopyrite ore
Pb-Zn ore
B)
A
A'
XQ09-3
XQ5, 7,10
XQ82, 86
XQ8
XQ10
XQ15
XQ25
XQ24
Permian-Triassic limestone
Qixia Fm limestone
Chuanshan Fm limestone
Huanglong Fm limestone
Gaolishan Fm sandstone
Wutong Fm sandstone
200 m
200 m
57°
quartz diorite
diorite porphyry
XQ5
sample location
and number

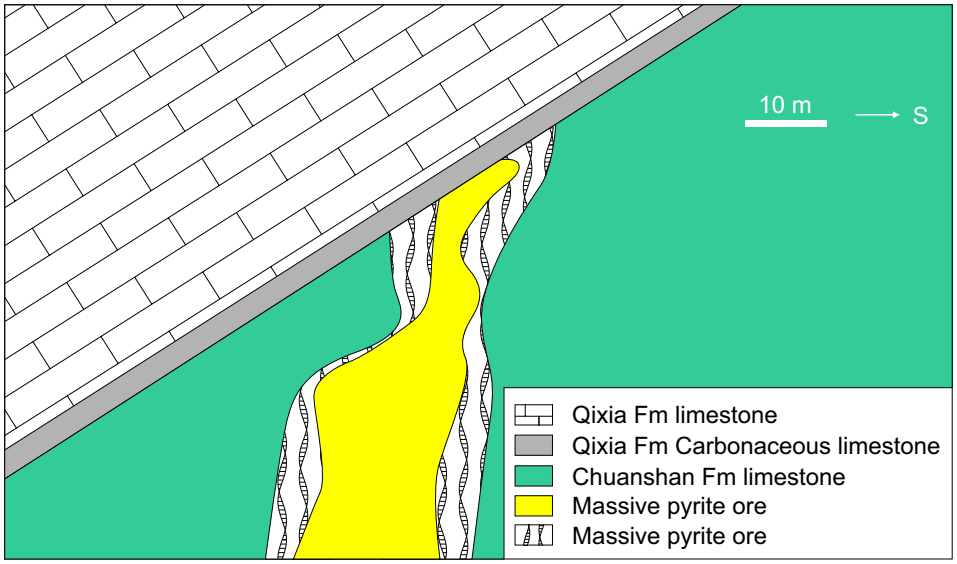
10 m
S
Qixia Fm limestone
Qixia Fm Carbonaceous limestone
Chuanshan Fm limestone
Massive pyrite ore
Massive pyrite ore

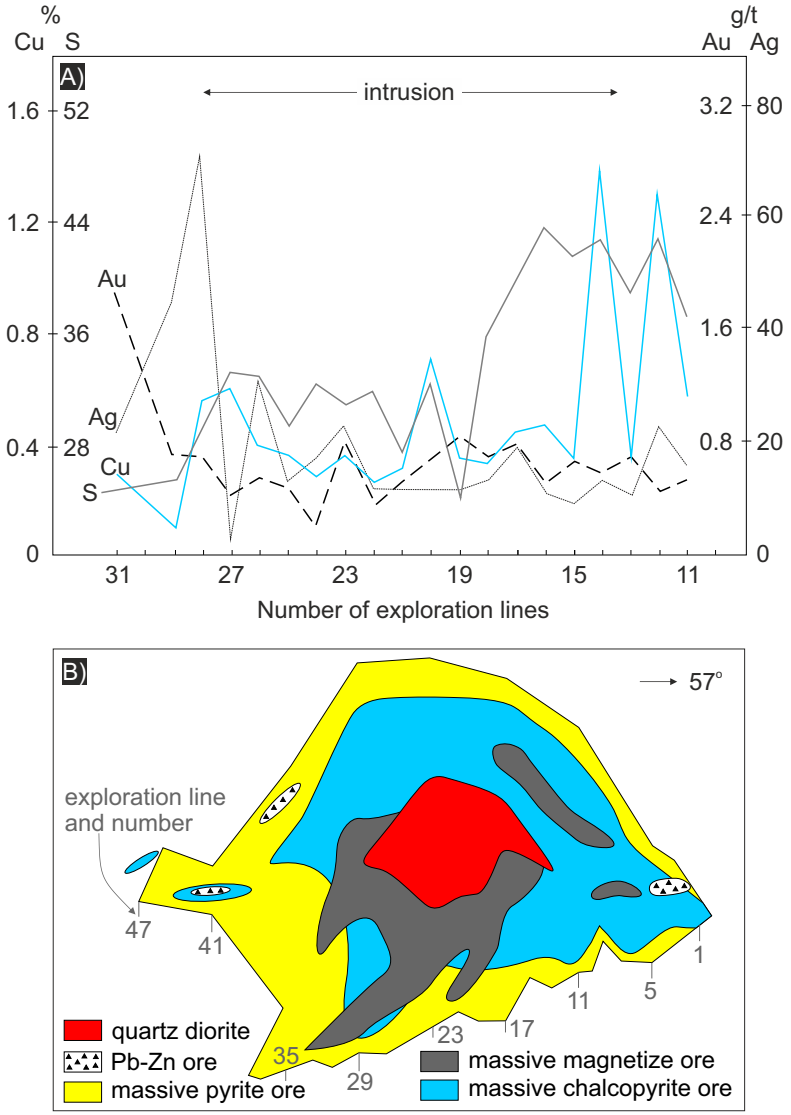
A)
%
Cu S
g/t
Au Ag
intrusion
1.6 52
1.2 44
0.8 36
0.4 28
0
3.2 80
2.4 60
1.6 40
0.8 20
0
Au
Ag
Cu
S
31 27 23 19 15 11
Number of exploration lines
B)
57°
exploration line
and number
47
41
35
29
23
17
11
5
1
quartz diorite
Pb-Zn ore
massive pyrite ore
massive magnetize ore
massive chalcopyrite ore

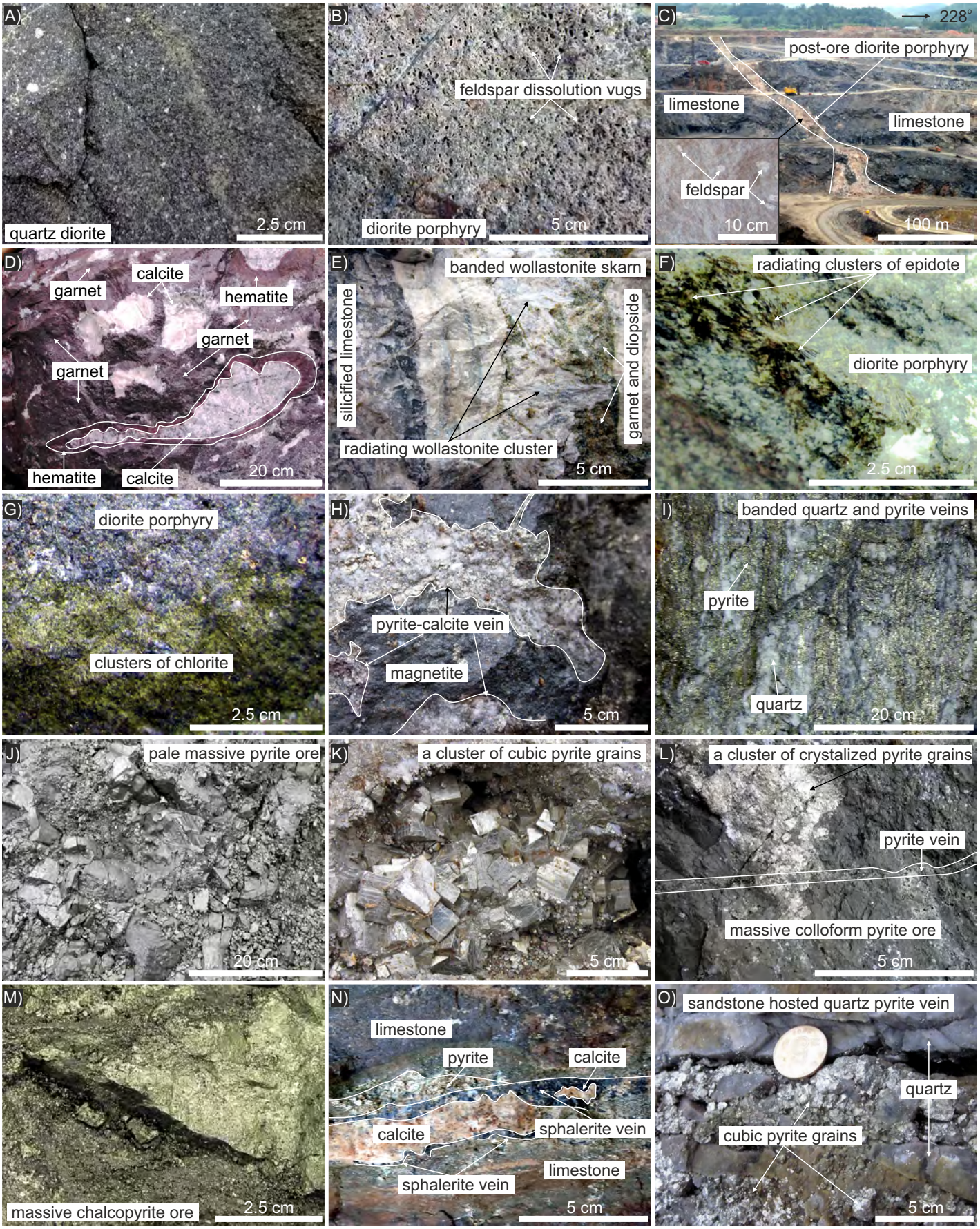
A)
quartz diorite
2.5 cm
B)
feldspar dissolution vugs
diorite porphyry
5 cm
C)
228°
post-ore diorite porphyry
limestone
limestone
feldspar
10 cm
100 m
D)
garnet
calcite
hematite
garnet
garnet
hematite
calcite
20 cm
E)
banded wollastonite skarn
silicified limestone
garnet and diopside
radiating wollastonite cluster
5 cm
F)
radiating clusters of epidote
diorite porphyry
2.5 cm
G)
diorite porphyry
clusters of chlorite
2.5 cm
H)
pyrite-calcite vein
magnetite
5 cm
I)
banded quartz and pyrite veins
pyrite
quartz
20 cm
J)
pale massive pyrite ore
20 cm
K)
a cluster of cubic pyrite grains
5 cm
L)
a cluster of crystalized pyrite grains
pyrite vein
massive colloform pyrite ore
5 cm
M)
massive chalcopyrite ore
2.5 cm
N)
limestone
pyrite
calcite
calcite
sphalerite vein
limestone
sphalerite vein
5 cm
O)
sandstone hosted quartz pyrite vein
quartz
cubic pyrite grains
5 cm

minerals	uneconomic skarn	mineralization stage
garnet		
diopside		
wollastonite		
epidote		
tremolite		
chlorite		
magnetite		
hematite		
sericite		
calcite		
quartz		
pyrite		
colloform pyrite		
chalcopyrite		
sphalerite		
galena		

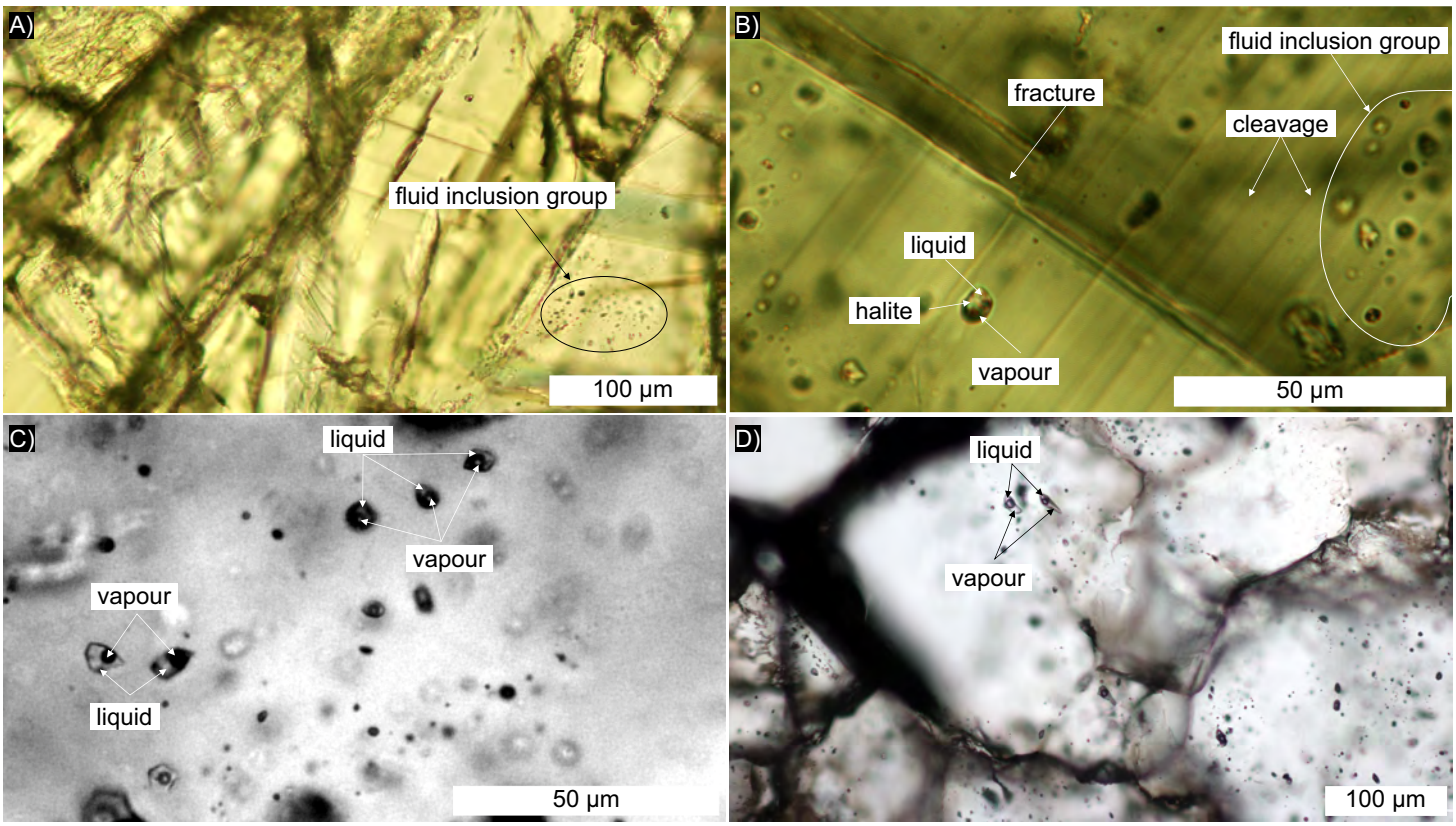
A)
fluid inclusion group
100 µm
B)
fluid inclusion group
fracture
cleavage
liquid
halite
vapour
50 µm
C)
liquid
vapour
vapour
liquid
50 µm
D)
liquid
vapour
100 µm

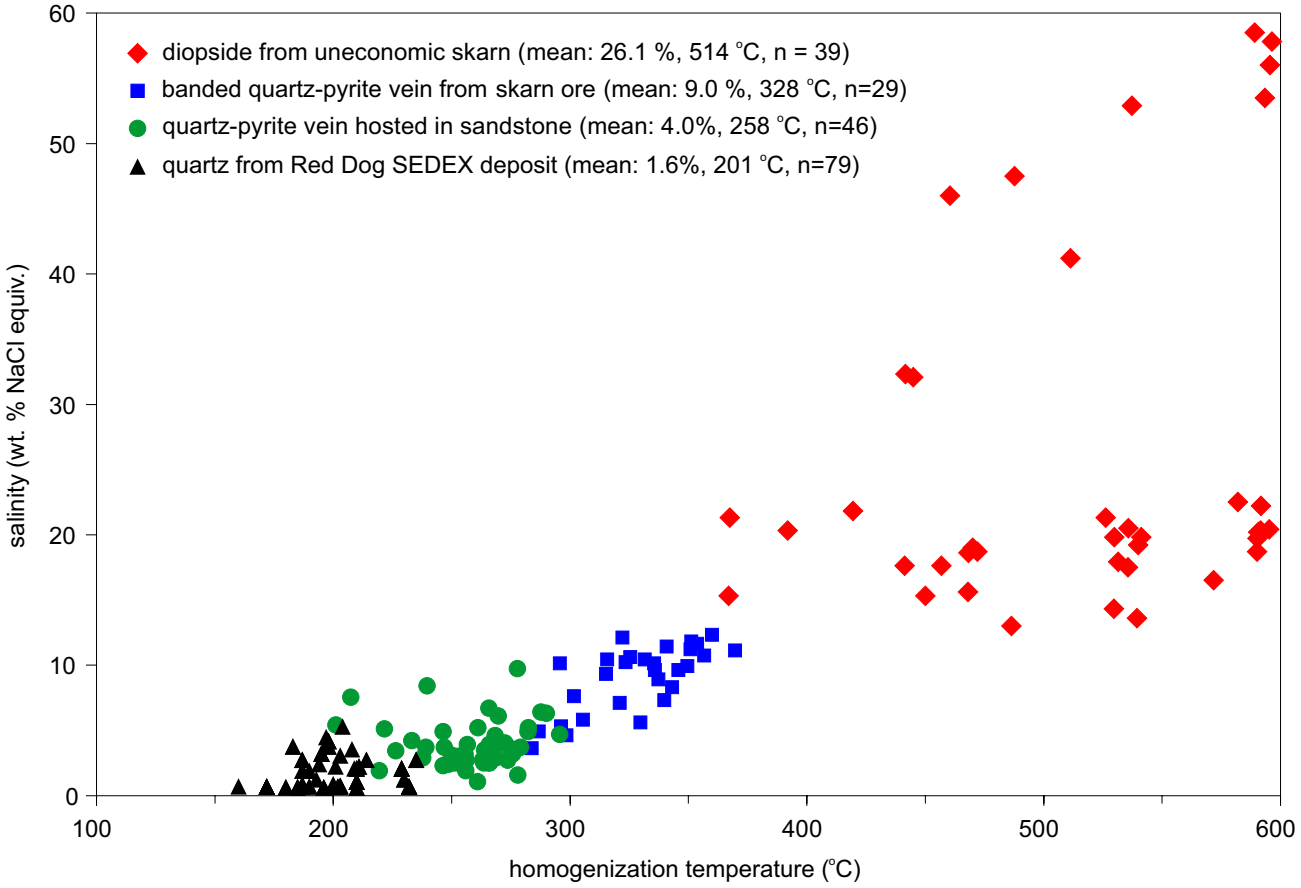
diopside from uneconomic skarn (mean: 26.1 %, 514 °C, n = 39)
banded quartz-pyrite vein from skarn ore (mean: 9.0 %, 328 °C, n=29)
quartz-pyrite vein hosted in sandstone (mean: 4.0%, 258 °C, n=46)
quartz from Red Dog SEDEX deposit (mean: 1.6%, 201 °C, n=79)
salinity (wt. % NaCl equiv.)
homogenization temperature (°C)
0
10
20
30
40
50
60
100
200
300
400
500
600

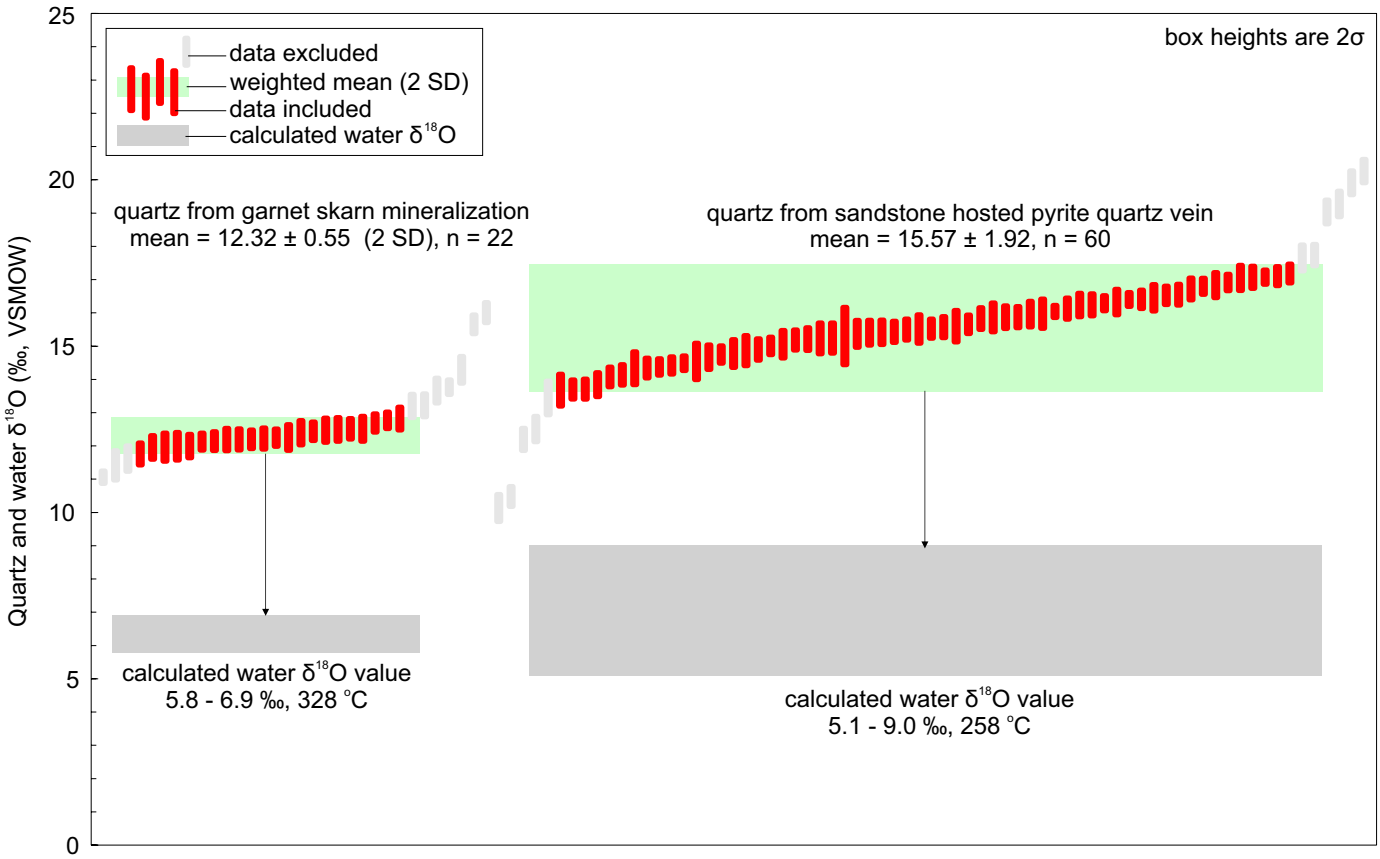
box heights are 2σ
data excluded
weighted mean (2 SD)
data included
calculated water δ18O
quartz from garnet skarn mineralization
mean = 12.32 ± 0.55 (2 SD), n = 22
quartz from sandstone hosted pyrite quartz vein
mean = 15.57 ± 1.92, n = 60
calculated water δ18O value
5.8 - 6.9 ‰, 328 °C
calculated water δ18O value
5.1 - 9.0 ‰, 258 °C
Quartz and water δ18O (‰, VSMOW)
25
20
15
10
5
0

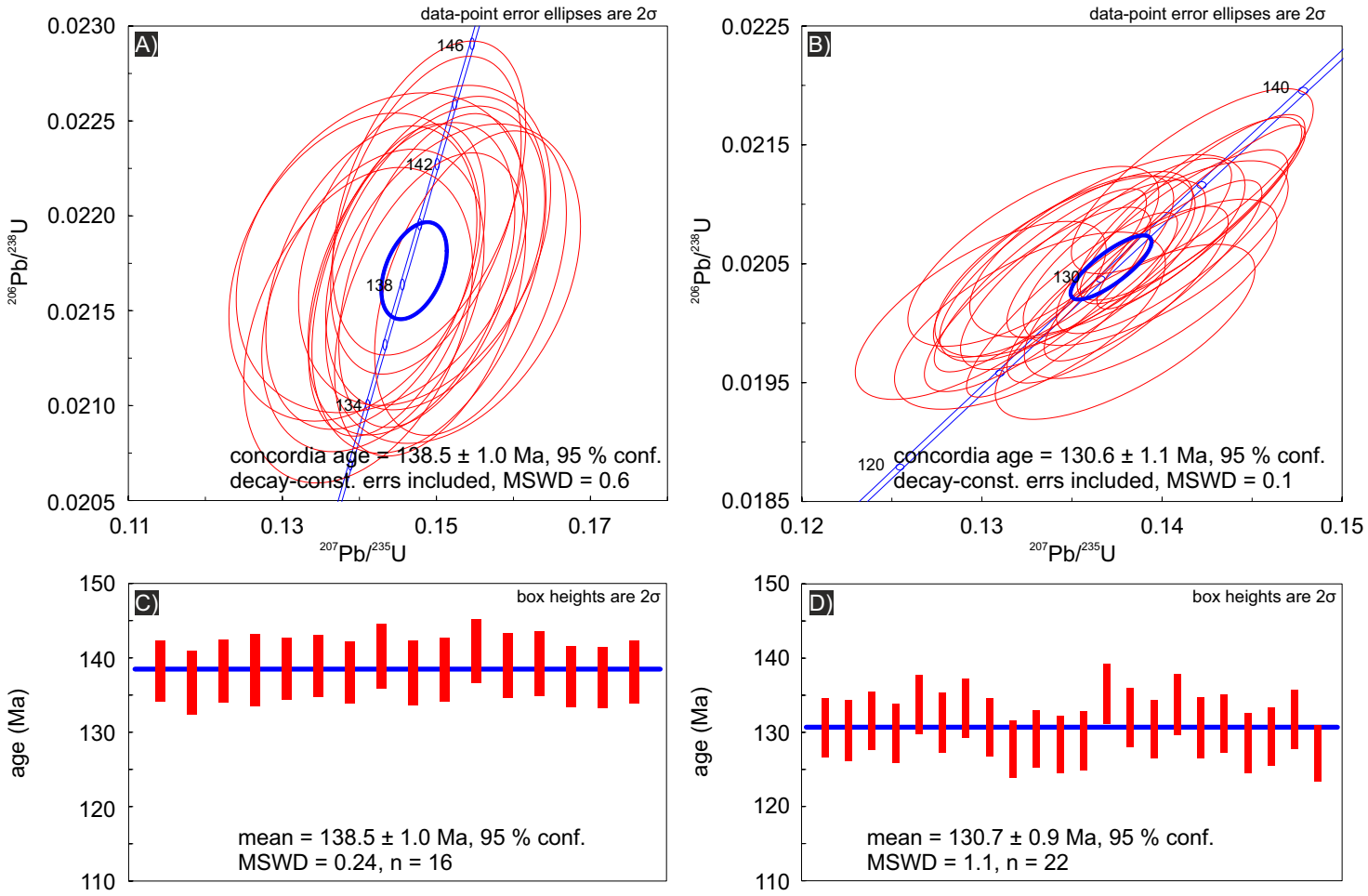
data-point error ellipses are 2σ
A)
146
142
138
134
concordia age = 138.5 ± 1.0 Ma, 95 % conf.
decay-const. errs included, MSWD = 0.6
0.0230
0.0225
0.0220
0.0215
0.0210
0.0205
0.11
0.13
0.15
0.17
206Pb/238U
207Pb/235U
data-point error ellipses are 2σ
B)
140
130
120
concordia age = 130.6 ± 1.1 Ma, 95 % conf.
decay-const. errs included, MSWD = 0.1
0.0225
0.0215
0.0205
0.0195
0.0185
0.12
0.13
0.14
0.15
206Pb/238U
207Pb/235U
C)
box heights are 2σ
mean = 138.5 ± 1.0 Ma, 95 % conf.
MSWD = 0.24, n = 16
150
140
130
120
110
age (Ma)
D)
box heights are 2σ
mean = 130.7 ± 0.9 Ma, 95 % conf.
MSWD = 1.1, n = 22
150
140
130
120
110
age (Ma)

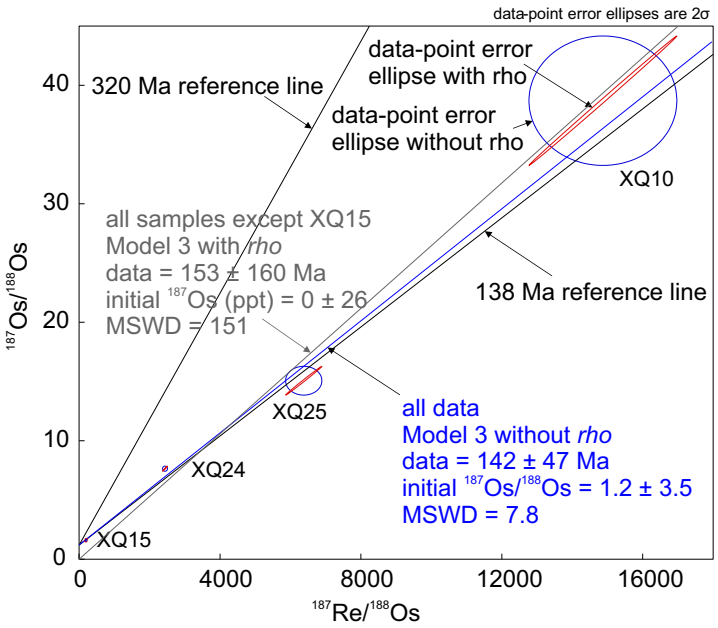
data-point error ellipses are 2σ
data-point error
ellipse with rho
data-point error
ellipse without rho
320 Ma reference line
XQ10
all samples except XQ15
Model 3 with rho
data = 153 ± 160 Ma
initial 187Os (ppt) = 0 ± 26
MSWD = 151
138 Ma reference line
XQ25
all data
Model 3 without rho
data = 142 ± 47 Ma
initial 187Os/188Os = 1.2 ± 3.5
MSWD = 7.8
XQ24
XQ15
0
10
20
30
40
0
4000
8000
12000
16000
187Os/188Os
187Re/188Os

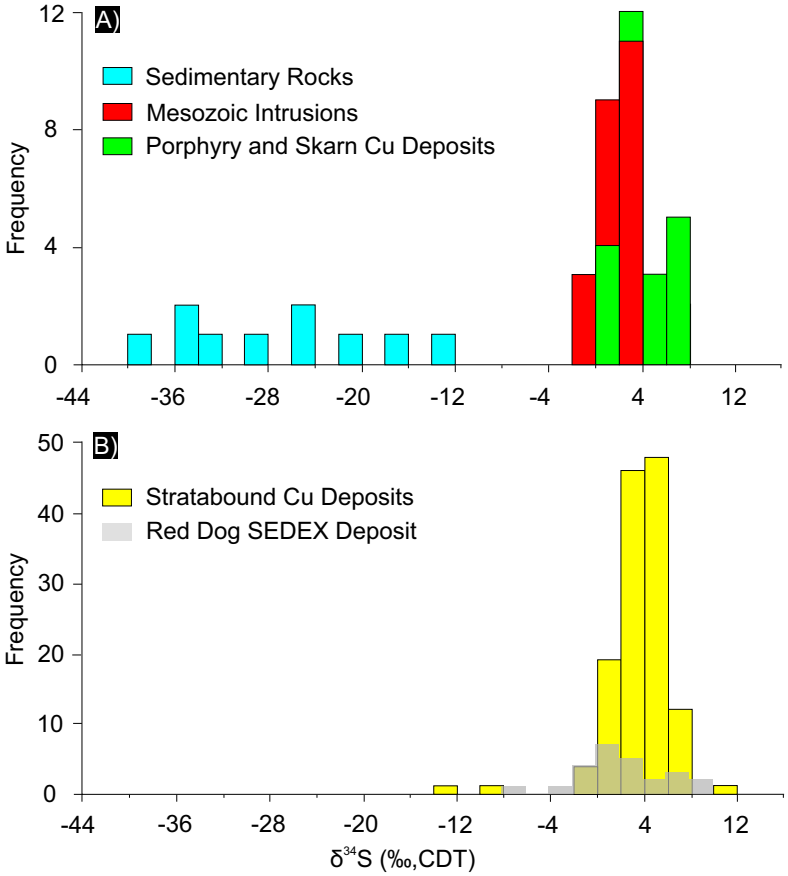
A)
Sedimentary Rocks
Mesozoic Intrusions
Porphyry and Skarn Cu Deposits
Frequency
12
8
4
0
-44
-36
-28
-20
-12
-4
4
12
B)
Stratabound Cu Deposits
Red Dog SEDEX Deposit
Frequency
50
40
30
20
10
0
-44
-36
-28
-20
-12
-4
4
12
δ34S (‰,CDT)

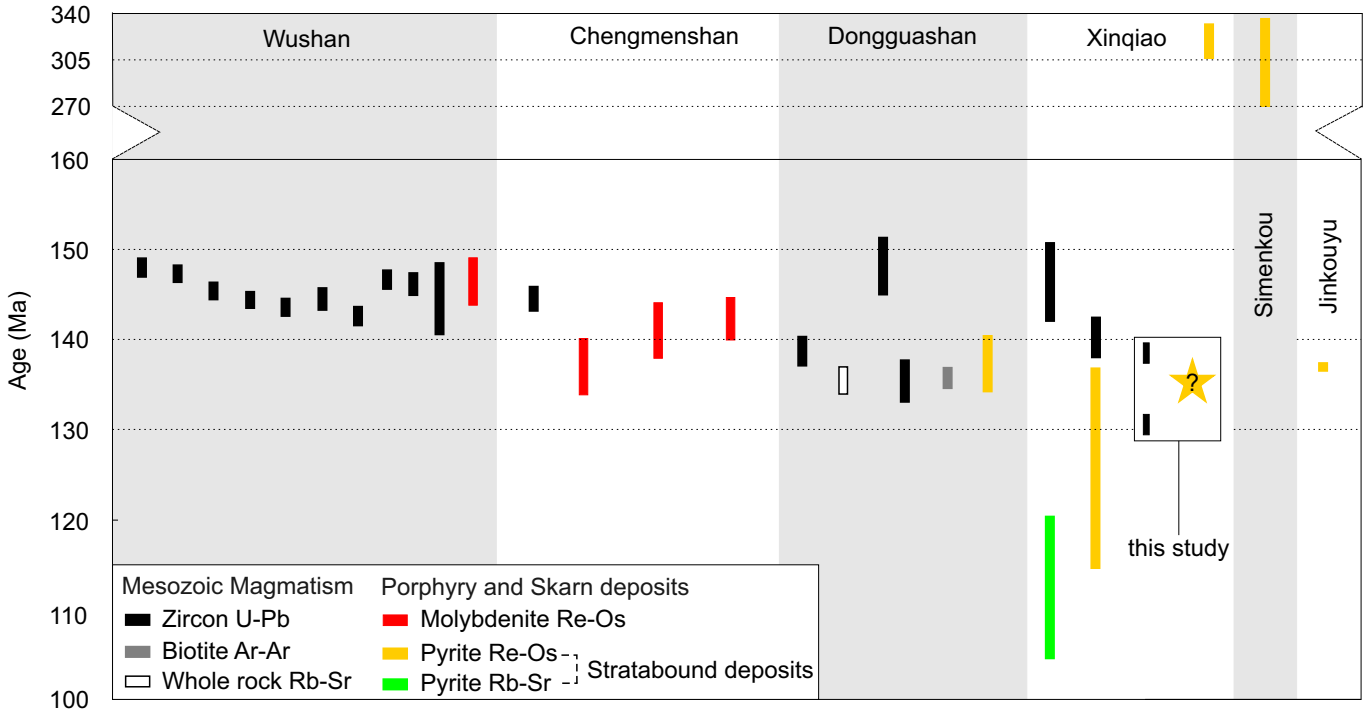
Age (Ma)
340
305
270
160
150
140
130
120
110
100
Wushan
Chengmenshan
Dongguashan
Xinqiao
Simenkou
Jinkouyu
?
this study
Mesozoic Magmatism
Zircon U-Pb
Biotite Ar-Ar
Whole rock Rb-Sr
Porphyry and Skarn deposits
Molybdenite Re-Os
Pyrite Re-Os
Pyrite Rb-Sr
Stratabound deposits

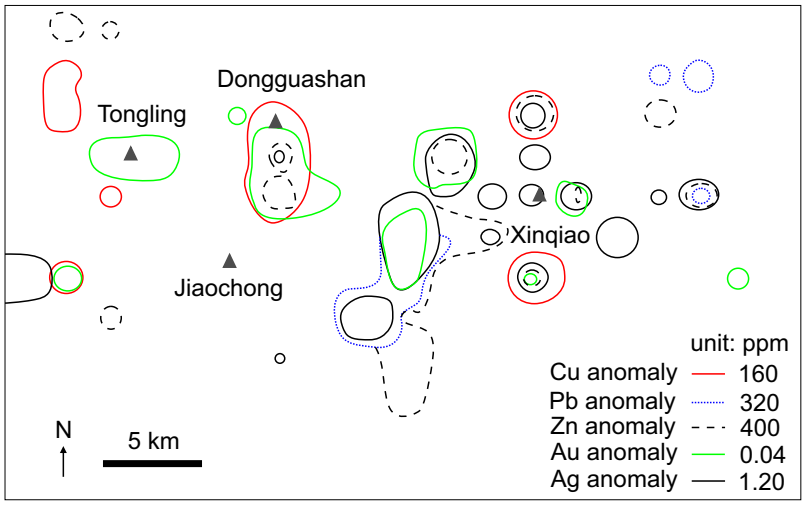
Dongguashan
Tongling
Xinqiao
Jiaochong
unit: ppm
Cu anomaly 160
Pb anomaly 320
Zn anomaly 400
Au anomaly 0.04
Ag anomaly 1.20
N
5 km